Rigidization capacity and folding behavior of variable stiffness composite skin for inflatable lunar habitats

Wang, Qinyu; Feng, Peng; Wu, Bo; Zhao, Jiacheng; Tang, Juntian; Jansen, Kaspar

DOI
10.1016/j.compositesa.2025.109169

Publication date
2025

Document Version
Final published version

Published in
Composites Part A: Applied Science and Manufacturing

Citation (APA)
Wang, Q., Feng, P., Wu, B., Zhao, J., Tang, J., & Jansen, K. (2025). Rigidization capacity and folding behavior of variable stiffness composite skin for inflatable lunar habitats. *Composites Part A: Applied Science and Manufacturing*, *199*, Article 109169. https://doi.org/10.1016/j.compositesa.2025.109169

Composites: Part A 199 (2025) 109169

Contents lists available at ScienceDirect

Composites Part A

journal homepage: www.elsevier.com/locate/compositesa

Rigidization capacity and folding behavior of variable stiffness composite skin for inflatable lunar habitats

Qinyu Wang [a], Peng Feng [a,*], Bo Wu [a], Jiacheng Zhao [a], Juntian Tang [a], Kaspar Jansen [b]

[a] Key Laboratory of Civil Engineering Safety and Durability of Ministry of Education, Department of Civil Engineering, Tsinghua University, Beijing 100084, China
[b] Department of Sustainable Design Engineering, TU Delft 2628 CE Delft, NL, the Netherlands

HIGHLIGHTS

- Dual-layer analytic model: rigidization capacity vs. stiffness & thickness ratios.
- Stiffness design principle for large shape change & flexible material reinforcement.
- CT reveals microscopic mechanism for post-folding softening & preserved strength.
- Folding endurance tests highlight resilience and safety margins of SC-AF material.
- Optimized FEM model integrates three-state stiffness membrane for lunar conditions.

ARTICLE INFO

Keywords:
Variable stiffness composite skin
Silicone-coated aramid fabric (SC-AF)
Post-folding softening
Rigidization capability

ABSTRACT

Lunar construction is challenged by harsh environments and limited resources. Inflatables, with their inherent adaptability, offer promising solutions. This study introduces rigidizable inflatable lunar habitats using silicone-coated aramid fabric (SC-AF) as restraint layer and shape memory polymer (SMP) for rigidization. SC-AF exhibits excellent mechanical stability, folding capability, and tear resistance. After one fold, stiffness dropped by 17 % with negligible strength loss. X-ray micro-computed tomography (μCT) analysis revealed fiber deformation, misalignment, and coating micro-cracks, while fiber integrity remained almost intact. After 500 folds, stress dropped 19 % and stabilized after 10,000 cycles. Even after 50,000 folds, the material retained 29 % of its original strength without major fiber rupture, confirming Kevlar's toughness. Practical applications involve fewer folds and less repetitive angles, allowing for a 20 % design safety margin. A theoretical dual-layer beam model evaluates equivalent stiffness based on material stiffness and thickness ratios, offering design limits and guidelines for rigidization and vibration control. For the SMP used, a thickness ratio of 0.02 or 1 is recommended, not exceeding 5. Rigidization capability should align with structural load-bearing requirements. This study integrates analytical, experimental, and numerical methods to advance high-strength restraint materials, examines folding-induced performance changes, and establishes design principles for SMP-based variable stiffness applications.

1. Introduction

The moon is Earth's closest natural satellite which can serve as a crucial stepping stone for human exploration of outer space. It allows for scientific studies in various fields like geology, astronomy, physics, and chemistry. Additionally, the moon presents opportunities for energy production and resource development, including rare materials like iron, aluminum, silicon, titanium, oxygen, hydrogen, carbon, helium-3, nitrogen, etc. The advancements and medical by-products resulting from space exploration also have economic and societal benefits. Furthermore, lunar exploration encourages international cooperation and holds potential for future commercial activities like space tourism [1]. In recent years, there has been a renewed global interest in lunar exploration due to advancements in space technologies and increased space activities [2]. Initiatives such as the Artemis Program by American National Aeronautics and Space Administration (NASA) and the International Lunar Research Station (ILRS) [3] by China and Russia, as well as the involvement of countries like Europe [4], Japan [5,6], South

* Corresponding author.
E-mail address: fengpeng@tsinghua.edu.cn (P. Feng).

https://doi.org/10.1016/j.compositesa.2025.109169
Received 24 April 2025; Received in revised form 4 July 2025; Accepted 7 July 2025
Available online 10 July 2025

Korea [7], and India, demonstrate the widespread engagement in lunar missions and scientific research.

As lunar missions transition toward exploitation and utilization, the construction of lunar bases becomes a crucial objective. However, the challenging lunar environments, characterized by low gravity, ultra-high vacuum, large temperature variations, high radiation, and limited resources, necessitates special materials, structures, and construction methods. Various proposals have been put forward, such as NASA's SinterHub [8], ESA's Lunar Outpost [9], and Huazhong University of Science and Technology's (HUST) Xuanwu lunar habitation scheme [10]. A review of lunar base concepts reveals a common structural model: an inner inflatable habitat enclosed by an outer protective layer. The outer structures, typically constructed from in-situ materials such as compacted regolith, regolith blocks, lunar concrete, or regolith bags [11], serve as protective shells or self-supporting enclosures. Inflatable structures have emerged as promising solutions [12] for lunar habitation module design due to their lightweight nature, high packing efficiency, low transportation costs, minimal on-site construction materials, breathability, low production costs, reliable deployment, self-correcting systems, strength, favorable dynamic and thermal responses, and adaptability to curved surfaces [13,14,15,16]. These inflatable modules also expand available space, offering high deployment ratios, airtightness, and activity areas for astronauts.

Air leakage from inflatable structures is unavoidable due to material permeability, connections, and potential punctures. To enhance long-term structural rigidity, rigidization technologies for the membrane structures must be incorporated. Rigidized membrane structures reduce reliance on internal pressure, prevent collapse, and enhance structural safety, durability, and repairability. As reviewed by Defoort, B. et al. [17], rigidization technologies for space gossamer structures, such as satellite antennae and solar sails, are typically divided into mechanical (pre-stress), physical (phase change), and chemical (resin polymerization) methods. Among them, physical rigidization methods are preferred for their simplicity, reversibility, low energy requirements, and suitability for ground testing and repeated use [17,18]. Shape memory polymers (SMPs) and their composites (SMPCs), which are widely used in aerospace [19], are typical materials for physical rigidization. SMPs offer advantages such as high compaction rates, design versatility, and the elimination of mechanical connectors. Their reversible shape-memory effect is critical for deployable structures such as solar sails and foldable arrays [20,21], and especially beneficial in precision structures like antenna reflectors where component shape directly affects functionality [22].

In our previous research [23], a proposed design for rigidizable lunar habitats outlined potential materials and design criteria. An optimal restraint material, silicone-coated aramid fabric (SC-AF) was developed, boasting enhanced flexibility, stability, and good resistance to temperature fluctuations and tearing. Notably, the impact of folding on tensile strength was significantly mitigated, although a softening effect was observed, resulting in a 17 % stiffness reduction without significantly affecting material strength [24]. Given that the restraint layer serves as the primary load-bearing component for pressurized inflatable structures, and woven fiber layers are prevalent for reinforcement in space structures, understanding the softening mechanism and folding impact is crucial for skin material design and optimization. This paper delves further into the rigidization capability, folding effects, and an improved numerical model for this variable stiffness skin. The key contributions are outlined as follows:

- **Rigidization capability:** A detailed analytical study was conducted on the rigidization capability of a dual-layer material using theoretical mechanical models. This model has been extended from a Euler-Bernoulli beam model to account for the influence of a variable stiffness material layer. The effects of stiffness ratio, thickness ratio, and temperature on the equivalent stiffness of the dual-layer material were explored, proposing application perspectives and limitations.
- **Material design principle:** Optimal parameter ranges for various applications were identified, providing a solid theoretical foundation for material and structural optimization. The study explores the distribution (covering both the amount and arrangement) principle of variable stiffness materials to facilitate optimal shape changes and structural reinforcement, particularly in rigidization of soft membrane materials. This work provides essential insights for future design applications.
- **Post-folding softening effect:** Post-folding softening mechanism was analyzed using micro-computed tomography (μCT), clarifying the reduction of stiffness while maintaining almost constant strength. This analysis aids in optimizing material design for future applications.
- **Folding endurance:** Progressive strength drops and gap generation at the folding hinge were observed after multiple folding cycles. This underscores the exceptional folding resilience and design safety margin of the SC-AF material, providing testing and research methods for similar materials.
- **Structural model:** An orthotropic material model was developed to numerically investigate the variable stiffness composite skin. The simulation also accounted for the stiffening effect of the silicone coating transitioning into a glassy state at extremely low temperatures, resulting in a three-state stiffness profile. This approach enables the simulation of the structural performance under varying lunar surface temperature conditions, thereby enhancing the accuracy and applicability of the simulations.

This paper is organized into seven sections. Section 2 introduces the conceptual design and material selection of rigidizable inflatable lunar habitats, summarizing our previous research. Section 3 quantitatively investigates the stiffness variation capabilities and proposes optimal material design for a dual-layer material, emphasizing applications in inflatable rigidization. A polyurethane-based shape memory polymer (SMP) is used for stiffness tuning. Section 4 delves into a quantitative examination of folding impact, confirming the SC-AF material's excellent folding endurance. Section 5 advances the numerical model to effectively simulate structural rigidization and environmental temperature variations. Finally, Section 6 provides important notes and Section 7 concludes this work and outlines future research directions. This paper combines analytical, numerical, and experimental methods to introduce a high-strength restraint material with superior folding properties, uncovering performance changes during folding and offering crucial insights for material optimization. It establishes design principles for SMP-based variable stiffness applications, providing a theoretical framework for potential uses.

2. Concept and material of rigidizable inflatable lunar habitats

2.1. Extendable lunar base concept and construction process

Inflatable habitats are commonly designed in the shape of pressure vessels, such as spheres, cylinders, or their derivatives [25]. This proposal introduces a classic ball-and-stick model that combines cylindrical and spherical basic units. Cylindrical units serve as connection and transit modules with a maximum of two airlock connections, while spherical units can accommodate multiple airlocks at different angles, allowing for the connection of multiple corridors. Various architectural complexes can be formed by combining these unit types, and additional modules can be easily added for expansion into larger bases. The construction process of self-inflatable lunar habitats involves four steps: inflation and expansion, rigidization, regolith coverage, and pressurization. SMP's glassy state represents high stiffness, while the rubbery state indicates flexibility. In the rubbery state, SMP allows for easy folding of the skin. After cooling down to the glassy state, the structure retains its folded shape tightly for stowage and transportation. Actuating SMP to the rubbery state again allows the structure to be inflated and

erected. Once SMP returns to the glassy state, the structure becomes rigid, significantly increasing its stiffness. This process of rigidization using SMP is reversible, allowing for multiple deployments and reusability. For inflatable lunar habitats, the rigidized inflatable structure is covered with a regolith layer, and the interior space is pressurized to 1 atmosphere (1 atm) for human activities.

2.2. Material selection

In previous research, through the review of existing lunar base concepts, we summarized a general mode of the lunar habitat, which consists of three main components: prefabricated core modules, inflatable structures, and in-situ material structures, as shown in Fig. 1(a) [26]. The repurposing of landers into core functional areas reduces on-site operations by reusing life support devices and protective systems. The outer in-situ material layer is used for protective shells and the inner inflatable structure establishes a habitable environment.

NASA's TransHab project, launched in 1997, aimed to develop a cost-effective and spacious inflatable capsule for astronauts in space stations. The capsule's skin comprises five functional layers: inner liner, bladder, restraint layer, micrometeoroid/orbital debris protection layer, and thermal protection layer, as shown in Fig. 1(b). The skin material needs to be lightweight, flexible, heat and radiation resistant, airtight, and easily rigidized [21,22]. The habitats consist of an inner inflatable structure for living and research spaces, and an outer layer of regolith (either regolith bricks or bags) for radiation protection, thermal insulation, and micrometeoroid impact resistance. The focus of this study is primarily on the restraint layer, as the regolith layer fulfills the functions of micrometeoroid, radiation, and thermal protection. The materials selected in this research have been listed in the following sections.

2.2.1. Outer protection

The outer protective shells were constructed using in-situ materials, typically derived from lunar regolith, such as compacted regolith, regolith bricks, and regolith bags. Our current investigation into lunar in-situ construction primarily focusses on two methods: utilizing solar-concentrated melting to create bricks [28] and employing regolith bag structures for large-scale construction [26]. The former technique involves concentrating sunlight with a Fresnel lens to melt and solidify lunar regolith, producing durable block-like construction materials. We have established a mobile 3D printing platform to study the two-dimensional forming process parameters of solar-concentrated melting, such as light intensity, movement speed, and line spacing, to validate the effectiveness and feasibility of this method. The regolith bag serves several functions, including thermal insulation, radiation protection, and micrometeorite resistance. These prefabricated regolith bags are connected to an airbag on Earth and expand together with the airbag upon reaching the lunar surface. The regolith bag structure is versatile, capable of constructing foundations, protective barriers, and the outer layers of inhabited structures.

2.2.2. Rigidization material SMP: thermo-elastic vs. viscoelastic material models

A flexible aramid fiber reinforced polymer (AFRP) is used to bear the main tension load, while smart materials, such as shape memory polymer (SMP), are used to strategically increase the inflatable structure's stiffness by controlling special material properties. SMP undergoes a transition between its glassy state (high stiffness) and rubbery state (low stiffness) based on the temperature. The stiffness variation between these two states can be significant, reaching up to 1000 times. The use of SMP simplifies the design by enabling large shape changes without complex mechanisms involving moving parts [23]. The combination of SMP resin and SMP-aramid skin forms a rigidizable composite skin for the inflatable structures. Moreover, SMP's shape recovery effect helps reduce residual stress and strain in the material, making it suitable for shape-changing structures and eliminating creases in the skin.

Previous research developed material models of a polyurethane-based SMP and SMPC (SMP resin and aramid fiber fabric) [23]. The SMP exhibits a transition from a glassy state to a rubbery state as the temperature increases, passing through a viscoelastic region. The glass transition temperature for these materials is determined to be 65 °C. During the glass transition range (50 °C to 65 °C), the elastic stiffness decreased by 96 %, while damping increased by a factor of 11. The thermoelastic and viscoelastic material models were developed for numerical analysis. The thermoelastic model only considers temperature-dependent behavior which simplifies numerical simulations. It utilizes the storage modulus curve at 1 Hz and ignores viscoelastic damping effects, as shown in Fig. 2(a). On the other hand, the viscoelastic model incorporates time- and temperature-dependent properties. Experimental data obtained at different temperatures and frequencies are mapped onto a master curve using the time–temperature superposition principle, as depicted in Fig. 2(b). The thermoelastic model is used for evaluating stiffness variation, whereas the viscoelastic model can simulate both stiffness and damping variation vs. time. In this research, the thermoelastic model is employed to verify the rigidization method, including static analysis and modal analysis, while the viscoelastic model is employed for full transient analysis of the proposed inflatable habitat under dynamic excitations [23].

2.2.3. Restraint material silicone-coated aramid fabric (SC-FC): elastic model

In previous research [24], an initial trial used a flexible aramid fiber reinforced polymer (AFRP) composed of Kevlar fiber and flexible epoxy resin to bear the main tension load. Later, an optimal material, silicone coating (*HBD1248 Silicone, Jiangxi Hebida, China*) with a designed usage temperature of −35 to 250 °C is was employed as a substitute for the flexible epoxy resin. This silicone coating was combined with a Kevlar 29 fiber plain woven cloth (1000D, 200 g) to form the restraint material SC-AF, resulting in improved flexibility, stability, thermal tolerance across a wide temperature range, as well as exceptional tearing and puncture resistance. Additionally, the folding impact, which led to a decrease in tensile strength, was significantly reduced. SC-AF demonstrated an elastic modulus of 12.2 GPa and an ultimate stress of 624.6

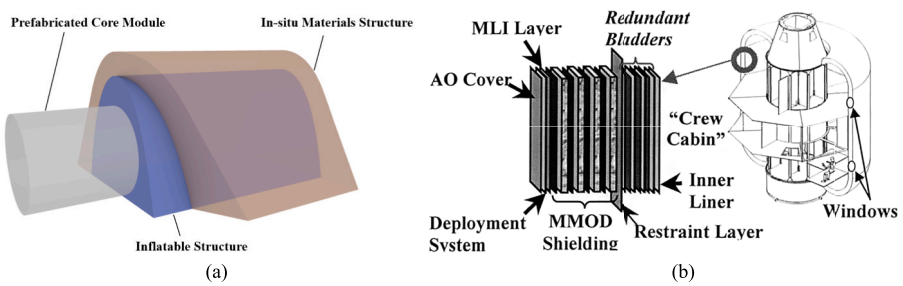

Fig. 1. (a)General mode of a lunar habitat [26]; (b)shell layers of TransHab habitation module [27].

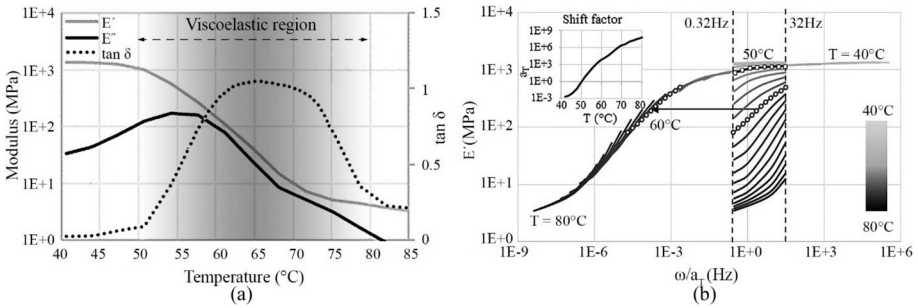

Fig. 2. SMP material characterization through DMA: (a) storage modulus (E′), loss modulus (E″), and material damping (tan δ) vs. temperature at 1 Hz; (b) master curve [23].

MPa. To model the flexible AFRP in the resistance layer, the computed laminate stiffness values were based on a four-layer stacking sequence of [0F/45F2/0F], which provided more uniform in-plane stiffness across all directions. In earlier simulations, an isotropic elastic model was used, which was reasonable for tensile conditions but insufficient for accurately simulating out-of-plane behavior. In this study, the Classical Laminate Theory (CLT) within the ACP module was employed to model the material using an orthotropic material model. This approach, detailed in Section 5, improves structural simulations by more accurately capturing stress distributions under various loading conditions.

3. Rigidization capacity and application opportunities & limits

3.1. Rigidization capability: analytic model of a dual-layer simply supported beam

Understanding how variable stiffness layers quantitatively influence structural performance (such as overall stiffness variation capacity, load-bearing capability, and deformation behavior) can effectively guide and optimize the design process. This knowledge enables the efficient selection of material properties and the development of design principles and processes for multilayer structures in various structural control applications, including rigidization, shape control, and even vibration control. By leveraging this understanding, the placement of variable stiffness materials (often smart materials, which are costly) can be optimized to achieve maximum efficiency and performance while minimizing material usage and cost.

To understand how the proportion of variable stiffness layers affects the overall stiffness of the composite skin, a theoretical model of a dual-layer simply supported beam is used, as shown in Fig. 3. In practical applications, for thin plates or membrane structures, the width is assumed to be very large, and in this analysis the out-of-plane deformation and torsion are neglected, simplifying the problem to a plane stress scenario. When a concentrated force F is applied at the center span of the beam (as shown in Fig. 3(a)), the beam typically experiences distinct stages of mechanical property changes: 1) **Linear elasticity with small deformation**, which determines the stiffness change; 2) **Ultimate state**, which determines the load-bearing capacity or large deformation capacity; 3) **Failure**, which is defined according to the relevant application criteria. The stiffness variation capacity of the beam is primarily determined during the first stage, where changes in modulus due to variable stiffness materials directly influence the beam's stiffness. Meanwhile, the second stage is critical for assessing the load-bearing capacity of the structure when the variable stiffness layer is in a rigid state, as well as the deformation capacity of the structure when the variable stiffness layer is in a flexible state. The detailed description and analysis of the beam are as follows:

3.1.1. Stiffness variation capacity

This stage determines the structure's capacity for stiffness variation. During this phase, the two material layers work together without interlayer misalignment. The deformation is small and the adhesive layer is securely bonded, the deformation adheres to the plane section assumption, and thus conforms to the Euler-Bernoulli beam theory. The stress and strain expressions are as follows:

Strain

$$\varepsilon(x,y) = (y - y_0)\phi(x) \tag{1}$$

Stress

$$\sigma(x,y) = E(y)\varepsilon(x,y) = \begin{cases} E_2(y - y_0)\phi(x) 0 < y < h_2 \\ E_1(y - y_0)\phi(x) h_2 < y < h_1 + h_2 \end{cases} \tag{2}$$

Where $\phi(x)$ is the bending curvature; E_1 is the stiffness of the upper layer Material 1 and h_1 is its thickness; E_2 is the stiffness of the lower layer Material 2, which may vary with actuation (e.g. thermally actuated as $E_2(T)$), and h_2 is its thickness, and the adhesive layer is assumed to be bonded without considering its thickness.

Let the neutral axis distance from the bottom surface in the dual-layer plate be y_0, and the width of the beam is b. The force equilibrium of the cross-section gives:

$$F(x) = \int_0^{h_1+h_2} \sigma(x,y) b dy = 0 \tag{3}$$

This leads to:

$$y_0 = \frac{E_2 h_2^2 + E_1 h_1^2 + 2E_1 h_1 h_2}{2(E_1 h_1 + E_2 h_2)} \tag{4}$$

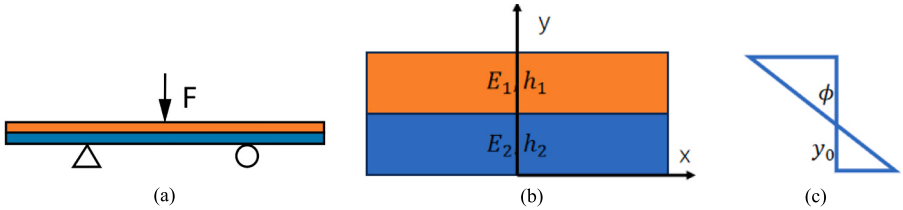

Fig. 3. Theoretic model of a dual-layer beam: (a) beam model; (b) cross-section and coordinate axes; (c) strain distribution along y direction, where y_0 is the height of the neutral axis.

Let the elastic modulus ratio $e = \frac{E_2}{E_1}$, and the thickness ratio be $t = \frac{h_2}{h_1}$. Then we have:

$$y_0 = \frac{1+2t+et^2}{2(1+et)}h_1 = h_2 + \frac{1-et^2}{2(1+et)}h_1 \tag{5}$$

When $t = \frac{1}{\sqrt{e}}$, it follows that $y_0 = h_2$.

For the equivalent bending stiffness, we define it as:

$$(EI)_{eq} = \frac{M(x)}{\phi(x)} \tag{6}$$

where $M(x)$ is the bending moment, expressed as:

$$\begin{aligned} M(x) &= \int_0^{h_1+h_2} \sigma(x,y)\cdot b y dy \\ &= E_2\phi(x)b\left(\frac{1}{3}h_2^3 - \frac{1}{2}y_0h_2^2\right) + E_1\phi(x)b \\ &\left(\frac{1}{3}(h_1+h_2)^3 - \frac{1}{3}h_2^3 - \frac{1}{2}y_0(h_1+h_2)^2 + \frac{1}{2}y_0h_2^2\right) \end{aligned} \tag{7}$$

Substituting Eq. (7) into Eq. (6) simplifies to:

$$(EI)_{eq} = \frac{1+4et+6et^2+4et^3+e^2t^4}{(1+et)}\cdot\frac{1}{12}bh_1^3E_1 \tag{8}$$

Thus, for different thickness ratios, varying E_2 can adjust the overall stiffness of the structure.

In practical applications, the variable stiffness capacity of these components should be maximized. However, since variable stiffness materials are typically expensive smart materials, their usage must be optimized for cost-effectiveness. Fig. 4 illustrates how the stiffness variation of a dual-layer component changes with the thickness ratio t and modulus ratio e of the two materials. The stiffness variation is defined as the ratio of the equivalent bending stiffness $(EI)_{eq}$, as shown in Eq. (8). The constant $\frac{1}{12}bh_1^3E_1$ has been eliminated, normalizing the stiffness change with respect to Material 1. Notably, the surface plot (3D graph) begins with a distinct "ridge" followed by a relatively long plateau. The ridge occurs around $e = 0.02$, indicating that adding just 2 % of the variable stiffness material to the bottom layer can effectively amplify the beam's stiffness by approximately threefold. The right figure reveals that the ridge curve exhibits a gradually diminishing stiffness variation rate, eventually stabilizing. This implies that the inherent stiffness-variation capability of the variable stiffness material (Material 2) is inherently limited, necessitating an optimal balance between material ratios. Critically, when Material 2's stiffness varies by 100-fold, the structural stiffness changes by about 2.5 times. A 400-fold stiffness variation in Material 2 increases the structural stiffness variation to 3.4 times, with a fourfold increase representing the practical upper limit. From Eq. (8), the stiffness variation increases proportionally to et^3. For $t = 0.02 = 2\times10^{-2}$, significant stiffness amplification begins when e exceeds the order of magnitudes approximately 10^6, beyond which the relationship transitions to linear growth. However, achieving such extreme modulus ratios ($e\sim10^6$) is impractical with real-world materials. This behavior highlights that variable stiffness primarily functions as a rigidizing role in this system, as Material 1 (a soft material) has a stiffness comparable to Material 2 in its flexible state.

In Section 3.2, SMP is used as an example to discuss real-world application scenarios. Once the materials are selected, the range of e is fixed, As shown in Fig. 4, the red curve on the surface represents this range, where the maximum elastic modulus ratio is $e_{max} = 406$. The process for determining the optimal t is discussed, and the optimization conditions are established to guide the subsequent design process. This section discusses the rigidization of flexible materials, which is mainly used for shape control of structures undergoing large deformations. In this case, the material becomes flexible to facilitate shape control and then stiffens afterward to enhance load-bearing capacity. Rigidizable membrane structures (such as inflatable structures discussed in the article) also fall into this category.

The discussion of ultimate states determines the structure's ultimate load-bearing capacity or large deformation capability, providing insight into how its strength improves in a stiff state and its deformation capacity in a more flexible state. There are two states of the variable stiffness material to analyze according to different applications: (1) stiff state for load-bearing; (2) flexible state for large deformation.

3.1.2. *Stiff state for load-bearing capacity*

During service, the dual-layer material is in the stiff state to bear loads. To assess the load-bearing capability, it is essential to analyze the beam's failure mechanisms, which are closely tied to the stiffness of the materials and adhesive layer. If the adhesive layer is strong and no delamination occurs, the beam will fail due to either tensile failure of the bottom material or compression failure of the top material, depending on which failure mode occurs first. If the adhesive is relatively flexible, failure may occur due to stress or strain exceeding the adhesive layer's limits, leading to delamination, interfacial failure, or mixed failure modes [29]. Given the complexity of failure modes and criteria, further discussion is deferred to case-specific material selection. The ultimate state is defined by the maximum mid-span load F_{es}. E_{max} and E_{min} represent the maximum and minimum elastic modulus of the beam, respectively. $(EI)_{eq,max}$ and $(EI)_{eq,min}$ represent the maximum and minimum equivalent bending stiffness of the beam, respectively. When Material 2 is stiff, with $E_{eq} = E_{max}$, the entire structure becomes rigid. Prior to failure, the beam remains in the small deformation range,

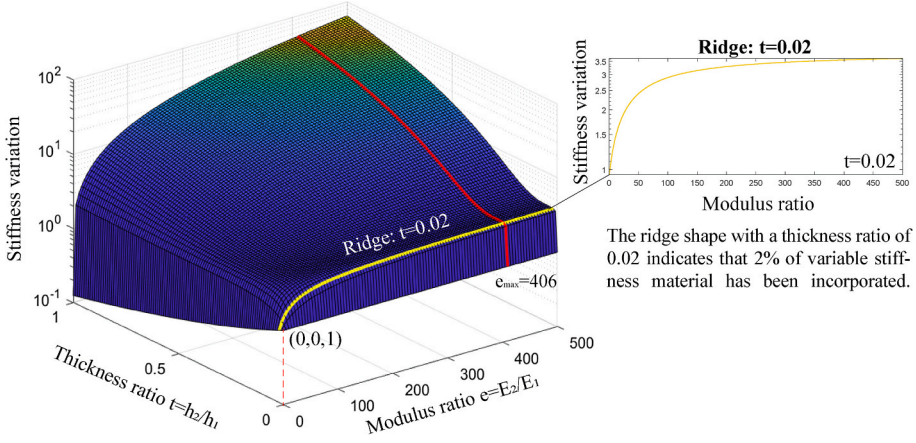

Fig. 4. Stiffness variation capacity vs. modulus ratio and thickness ratio.

exhibiting nearly elastic behavior until it reaches the ultimate load-bearing state. At this point, the increase in load-bearing capacity is given by:

$$\frac{F_{es}}{F_{ef}} = \frac{(EI)_{eq,max}}{(EI)_{eq,min}} = \frac{E_{max}}{E_{min}} \tag{9}$$

where F_{es} and F_{ef} represent the maximum load at mid-span under the same ultimate displacement when Material 2 is in the stiff state and flexible state, respectively (referring to the displacement at which F_{es} reaches the ultimate load-bearing capacity, while still remaining within the small deformation range). Further discussion on application limits is provided in Section 3.2 below.

3.1.3. Flexible state for large deformation

For variable stiffness components, the dual-layer material transitions to a flexible state to accommodate large shape changes (e.g., reconfiguration, expansion, or inflation). In this state, large deformation theory must be applied, as it accounts for changes in base-to-base distance while maintaining constant component length, unlike small deformation assumptions which neglect beam length variations. The deformation capability is quantified as the ratio of maximum mid-span deflection in the flexible state to that in the stiff state. The governing equations for in-plane large deformations of a slender beam are given by Eq. (10) [30]:

$$\begin{cases} x = \int_{\theta=\alpha}^{\theta=0} -\dfrac{cos\theta}{\sqrt{\dfrac{2}{EI}\left[F_y(sin\theta - sin\alpha) + F_x(cos\theta - cos\alpha)\right] + \left(\frac{M}{EI}\right)^2}}\, d\theta \\ y = \int_{\theta=\alpha}^{\theta=0} -\dfrac{sin\theta}{\sqrt{\dfrac{2}{EI}\left[F_y(sin\theta - sin\alpha) + F_x(cos\theta - cos\alpha)\right] + \left(\frac{M}{EI}\right)^2}}\, d\theta \end{cases} \tag{10}$$

where (x, y) represents the mid-span position, and α represents the angle change along the beam from the support to the mid-span. θ is the angle between the section along the beam and the horizontal axis (x axis). F_x, F_y, and M are the horizontal and vertical reaction forces and reaction moment, respectively. EI here represents the bending stiffness of the beam, equal to the equivalent bending stiffness $(EI)_{eq}$ in eq. (6).

For the force model in this study, the simply supported beam yields $M = 0$ at both ends, and the right end is free to slide horizontally, resulting in $F_1 = 0$. For half-span equilibrium, the vertical reaction force at the base is $F_2 = -F/2$ (negative sign indicates an upward force). With these constraints, Equation (10) simplifies to:

$$\begin{cases} x = \int_{\theta=\alpha}^{\theta=0} -\dfrac{cos\theta}{\sqrt{-\dfrac{F(sin\theta - sin\alpha)}{EI}}}\, d\theta \\ y = \int_{\theta=\alpha}^{\theta=0} -\dfrac{sin\theta}{\sqrt{-\dfrac{F(sin\theta - sin\alpha)}{EI}}}\, d\theta \end{cases} \tag{11}$$

Since the beam length remains unchanged, integration along its length coordinate must yield half of the total length:

$$\int_{\theta=\alpha}^{\theta=0} -\frac{1}{\sqrt{-\frac{F(sin\theta - sin\alpha)}{EI}}}\, d\theta = \frac{L}{2} \tag{12}$$

By solving Equations (11) and (12) simultaneously, the mid-span position (x, y) and angle α can be obtained. Since the integrand involves the square root of trigonometric functions, there is no simple analytical solution in elementary functions. Typically, numerical methods such as the rectangle method, trapezoidal rule, Simpson's rule, Gaussian quadrature, adaptive quadrature, and Monte Carlo integration are used for solving such equations. This study adopts an adaptive quadrature method, which dynamically adjusts the integration intervals based on local function variations.

Assuming the dual-layer beam has an elastic modulus of $E_1 = E_{2min} = 3.3$ MPa, with a rectangular cross-section of 20 × 5 mm and a beam length of 1000 mm, and considering a force range of [0.0001, 0.05] (N), the relationship between F, x, y, and α can be obtained by solving Equations (11) and (12). The relationships between these variables within this range are illustrated in Fig. 5, where x, y, and α are represented by black, grey solid, and grey dashed curves.

In the flexible state where $E_{eq} = E_{min}$, the adhesive layer is typically designed to be flexible as well, allowing it to accommodate the structural deformation. Both material layers can withstand significant deformation without failure. However, if the deformation exceeds the adhesive layer's strain or stress limits, delamination occurs, preventing the layers from working together—this is defined as failure in the flexible state. While layered materials can fail earlier than delamination (e.g., material rupture), such cases are relatively rare. To determine the maximum allowable deformation, the first occurring failure mode (e.g., material failure or delamination) is identified, and the corresponding deformation defines the limit. This deformation corresponds to the mid-span position (x_{max}, y_{max}), and the maximum deflection in the flexible beam is denoted as $\omega_{ef} = y_{max}$. Meanwhile, the maximum deflection in the stiff beam is defined as $\omega_{es} = \omega_{max} = \frac{F_{es}L^3}{48(EI)_{eq,max}}$. Thus, the increase in deformation capability is quantified as:

$$\frac{\omega_{ef}}{\omega_{es}} = \frac{y_{max}}{\omega_{max}} = \frac{48(EI)_{eq,max}}{y_{max}F_{es}L^3} \tag{10}$$

This also demonstrates that when shape control requiring large deformation is needed, transitioning Material 2 from the stiff to the flexible state enables the structure to shift from a small deformation to a large deformation.

3.2. Application opportunities & limits: rigidization of flexible membrane (including inflatables)

Considering the variable stiffness material model (thermoelastic) [31], E_2 is temperature-dependent and should be expressed as $E_2(T)$. For the SMP used in this study, during the state transition from 40 °C to 85 °C, the modulus decreased from $E_2(T_s) = 1340$ MPa to $E_2(T_f) = 3.3$ MPa, resulting in a stiffness variation factor of 1340/3.3 = 406 times. Since SC-AF is an anisotropic material, its bending stiffness is primarily influenced by the stiffness of the resin or coating. Compared to other membrane materials, such as TPU and Kapton, E_1 is set at 1340 MPa, giving $e_{min} = 1$ and $e_{max} = 406$. The relationship between stiffness variation and the thickness ratio t is depicted by the red curve in the surface plot of Fig. 4, which is re-plotted in Fig. 6 in both linear and logarithmic scales. As previously discussed in Section 3.1.1, the stiffness variation increases rapidly with a small addition of Material 2. When the material ratio reaches approximately 2 %, a distinct "ridge" appears, making an efficient design point where the stiffness variation is around 3.6 times. Beyond this point, the curve levels off into a plateau, and further increases in the amount of Material 2 do not significantly enhance stiffness variation. Therefore, it is advisable to avoid this range

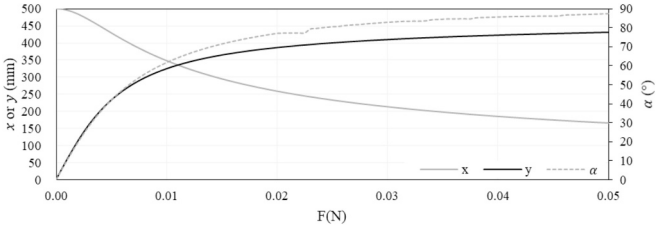

Fig. 5. Force vs. deformation (mid-span position (x, y) and angle change α) under large deformation.

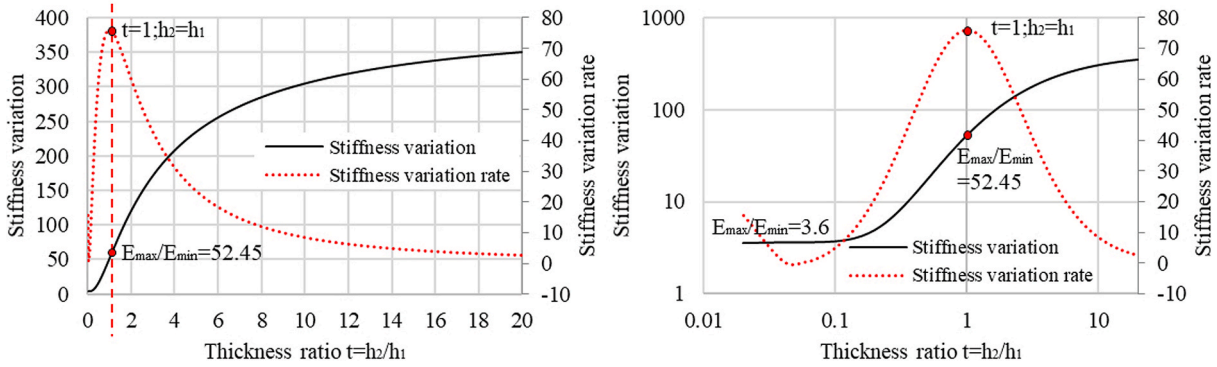

Fig. 6. Stiffness variation capacity and variation rate vs. thickness ratio; where $e_{max} = 406$. (a) and (b) linear and logarithmic scales.

during design, which spans roughly from $e = 0.02$ to 0.15, as shown by the black curve in Fig. 6(b). After the plateau, as the proportion of Material 2 increases, the stiffness variation of the dual-layer simply supported beam gradually increases, with an accelerating rate of change. As indicated by the red curves, Material 2 is most efficiently utilized for stiffness variation when the change rate peaks. This optimal design point occurs at $t = 1$, where both materials have equal thicknesses. At this optimal design point, the structure's stiffness variation capacity reaches a factor of 52. However, beyond this point, as more Material 2 is added, the material's efficiency gradually decreases, as the rate of change slows down. It is therefore suggested to avoid values of $e > 10$, as this leads to a significant waste of Material 2. It is recommended to keep e no more than 5, where the stiffness variation capability reaches a factor of 200. The upper bound of stiffness variation is 406, corresponding to the pure stiffness variation of Material 2.

Typically, when adding Material 2 enhances the structure's load-bearing capacity and the structure is intended for large deformations, with load-bearing capacity being the primary performance criterion, the stiffness of Material 1 should not be excessively high. Moreover, the modulus E_1 should be on the same order of magnitude as $E_{2,min}$ (in the flexible state), but much smaller than $E_{2,max}$ (in the rigid state). Under these conditions, Material 2 primarily contributes to the rigidization of flexible layers, such as membrane materials. As mentioned above, the recommended values for the thickness ratio t are 0.02 or 1, but should not exceed 5. The designed rigidization capability depends on the required load-bearing capability of the structure. As indicated in Eq. (9), the increase in load-bearing capability is equal to the stiffness variation ratio. The recommended values are listed in Table 1, and these values will be used to optimize the design of a rigidizable inflatable habitation unit [32], as discussed in Section 5.

4. Folding impact of silicone-coated aramid fabric (SC-AF)

4.1. Monotonic uniaxial tensile test

The elastic modulus and tensile strength of SC-AF were measured through an Instron universal tester (100kN) and a *Wance* universal tester (250kN) equipped with capstan tensile grips, respectively, as shown in Fig. 7 (a) and (b). Two groups of specimens with five samples each were prepared for the tensile tests: unfolded and folded. All tensile tests were conducted in accordance with the GB/T3923.1–2013 standard. [24].

Fig. 8 illustrates the force–displacement and stress–strain curves of unfolded and folded fabric specimens for strength and modulus measurements. Initially, there is a gradual slope before entering the linear region, which can be attributed to the relative relaxation of the material when clamped. During initial stretching, the material was straightened until fully taut, and then it began to exhibit linear elasticity. During the strength measurement, the material demonstrated elasticity initially, but it abruptly ruptured at around 600 MPa before any substantial damage occurred. On the other hand, during the modulus measurement at approximately 300 MPa, the specimen began to slip out of the clamps as the stress increased. Consequently, the stress dropped, and a further increase became unattainable. Table 2 reports the average results of five specimens from tensile tests conducted on SC-AF specimens, including elastic modulus, elongation at break, ultimate stress, and ultimate load. The modulus was determined using the $\Delta\varepsilon = 0.5$ % chord modulus from the middle range of the stress–strain curves. A strain range of 2.5 % to 3 % yielded favorable outcomes for both unfolded and folded groups. Upon folding, the average elastic modulus dropped by 16.6 % from 12.2 GPa to 10.1 GPa, the ultimate load and stress also experienced reductions of 2.96 % (from 7.73 to 7.5kN) and 6.63 % (from 624.6 to 583.2 MPa), respectively. However, the elongation at break remained nearly unchanged before and after folding, measuring 15.5 % and 15.3 %, respectively.

Fig. 7(c) depicts the failure modes of unfolded and folded specimens. In unfolded specimens, damage occurred unpredictably in various areas. Two types of failure modes were observed: one with a fracture surface perpendicular to the tension direction (observed in specimens 1, 2, and 5 in Fig. 7(c)), and the other with an inclined fracture surface (observed in specimens 3 and 4 in Fig. 7(c), at an angle of approximately 40° relative to the tension direction). Both failures initiated at the edge fibers and propagated inward until the crack extended across the transverse section. The inclination in the fracture surfaces can be attributed to the initial misalignment of the specimens with respect to the tension direction, causing eccentricity and shear stress during stretching. Despite possible experimental imperfections, the ultimate force and stress values for specimens 3 and 4 fell within the average range, indicating minimal impact on the overall test results. In contrast, folded specimens mostly exhibited damage at the crease location (as observed in specimens 1, 2, and 4 in Fig. 7(c)), resulting from local stress concentration due to folding. Although the fracture locations of specimens 3 and 5 were not at the crease, their ultimate force and stress values also fell within the average range, confirming their validity in the experimental results.

In previous research [24], a magnified photograph (Fig. 7(d)) of the folding area of an SC-AF specimen showed the silicone coating turning white at the crease, with some microcracks present. Folding leads to damage and buckling in the coating, causing local delamination between the coating and fiber cloth, despite Kevlar fiber's excellent anti-fatigue properties and the resin's flexibility. Considering that the modulus of the material decreased by up to 16.6 %, which exceeds the proportion of the contribution of the silicone rubber coating, it suggests some softening effects in the aramid fibers after folding. However, no

Table 1
Recommended usage of SMP layer and rigidization capability (stiffness variation and load-bearing).

Thickness ratio $t = h_2/h_1$	2 %	1	2	3	4	5
Stiffness variation & load-bearing capabilities	3.56	52.4	121.5	172.2	208.6	235.6

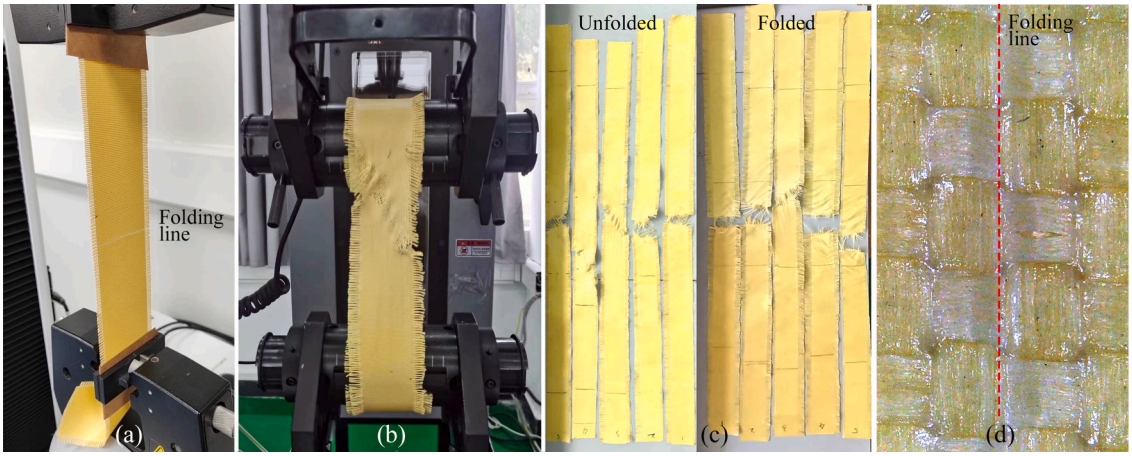

Fig. 7. Test setups: (a) folding treatment for five specimens for one week; (b) capstan tensile grips on a Wance universal tester (250kN); (c) specimen in capstan tensile grips for ultimate strength measurement; (d) folded specimen in pneumatic grips on an Instron universal tester (100kN) for module measurement. [24].

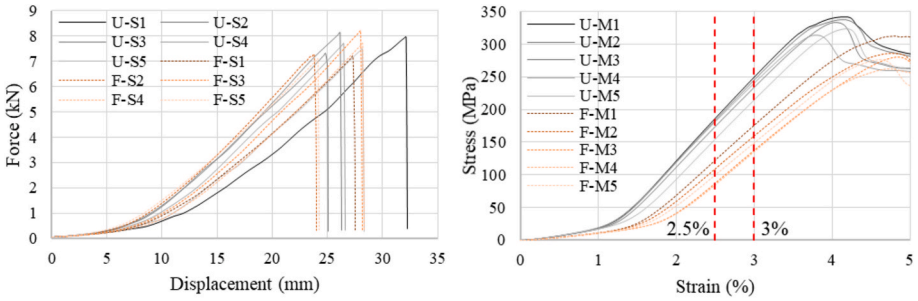

Fig. 8. Tensile test results: unfolded vs. folded: (a) Strength measurement: force vs. displacement; (b) modulus measurement (2%-3% chord modulus): stress vs. strain.

Table 2
Tensile test results of unfolded and folded specimens: elastic modulus, elongation at break, ultimate stress, and ultimate load.

Group	Modulus E (GPa)	Elongation at break (%)	Ultimate Stress σ_{UIT} (MPa)	Ultimate Load F_{UIT} (kN)
Unfolded	12.2	15.5	624.6	7.73
Folded	10.1	15.3	583.2	7.50
Reduction (%)	16.6	1.07	6.63	2.96

significant damage was observed in the fibers, as indicated by the nearly unchanged ultimate strength and elongation of the material. This stiffness reduction of the coated fabric may be attributed to fiber deformation and misalignment after folding, as well as local buckling and microcracks in the silicone coating. These factors lead to decreased fiber alignment during tension, ultimately resulting in a softening effect.

4.2. Mechanism of post-folding softening effect

4.2.1. X-ray micro-computed tomography (μCT) observation at micro-scale

To quantitatively investigate stiffness reduction, this section further explores the softening mechanism using micro-CT. Two small square specimens of the SC-AF sample were extracted from the folded and unfolded regions for scanning, as illustrated in Fig. 9(a). Three areas were analyzed: unfolded region (U), inside folded region (IF), and outside folded region (OF). A 2 mm × 2 mm area, approximately the width of two filament bundles, was scanned at a resolution of 2.078 μm. Representative cross-sectional images were obtained by slicing along the thickness and height directions, as shown in Fig. 9(b)~(g). At the given resolution, individual filaments are clearly visible, with lighter regions indicating fiber structures.

In general, the folded region (Fig. 9(b)~(e)) exhibited lower fiber density, overall volume expansion, and a sparser fiber distribution compared to the unfolded region ((Fig. 9(f) and (g)). Additionally, the inside folded region (Fig. 9(b) and (c)) showed greater fiber sparsity and expansion than the outside folded region ((Fig. 10(c) and (d)). The coating in the inside folded region was damaged, which can be observed from Fig. 10(c), where the surface appeared rough and discontinuous. Interlayer cross-sections also revealed some pores, but no obvious fiber fractures or damage were observed in the inside folded region. In contrast, the unfolded region had a denser, more uniform fiber distribution with a smaller overall volume (Fig. 9(d) and (e)).

4.2.2. Quantitative analysis

To further analyze fiber morphology, the scanned fibers were rebuilt and simulated to evaluate the deformation of fiber segments using tortuosity as a quantitative metric, as shown in Fig. 10. A term of ***Tortuosity*** τ is used, which describes the degree of deviation of a curved path from a straight line. It is defined as:

$$\tau = \frac{L}{L_0} \tag{12}$$

where L is the actual curved length of the fiber segment, and L_0 is the chord length (straight-line distance) between the segment's endpoints. A higher τ value indicates a more tortuous, deformed fiber path.

The results indicate significant deformation within the folded region, with deformation gradually decreasing along the thickness direction from the inside to the outside of the folding crease. The outside exhibited

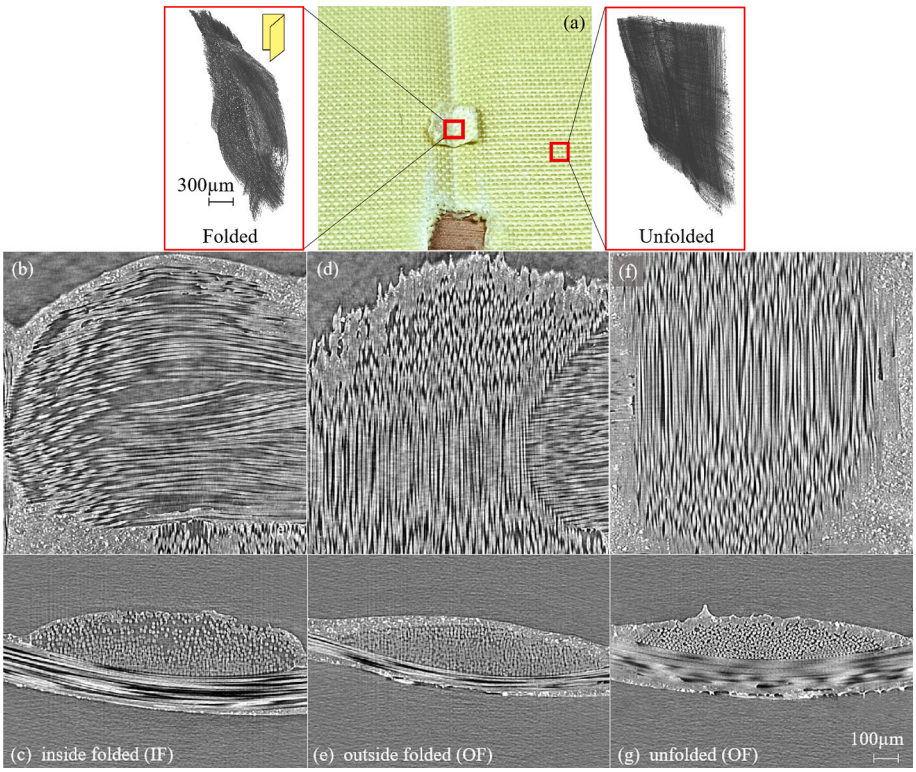

Fig. 9. (a) X-ray CT specimen of the folded SC-AF; (b) and (c) two views of CT photos for the inside of folded region; (d) and (e) the outside of folded region; (f) and (g) unfolded region.

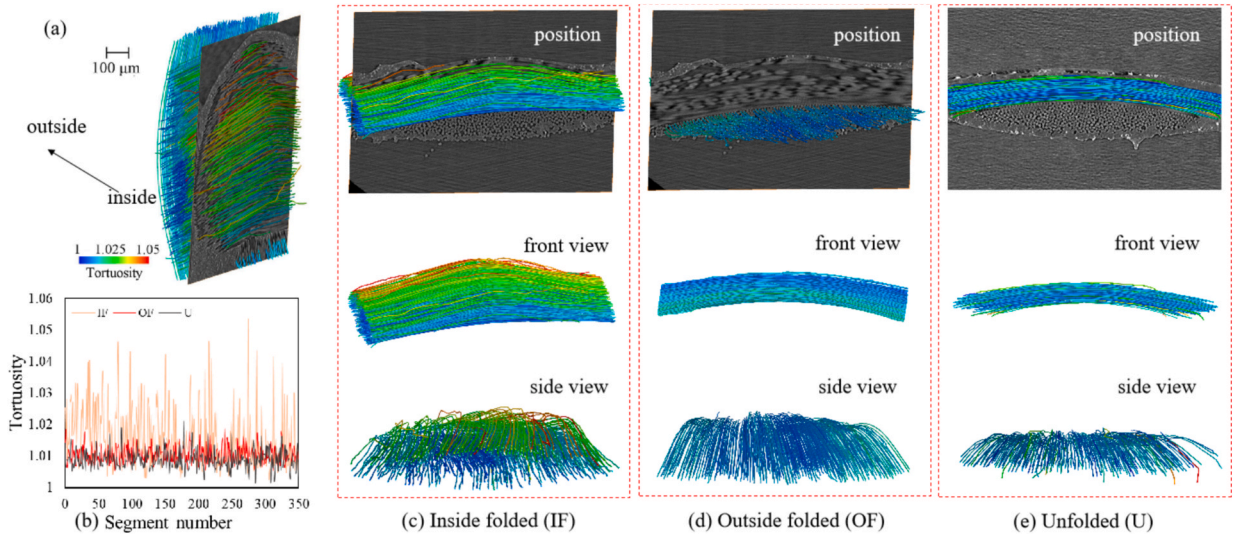

Fig. 10. (a) filament orientations from inside to outside of folded region; (b) tortuosity of fibers from IF, OF, and U regions; (c), (d), and (e) simulated filaments of inside folded, outside folded, and unfolded regions.

minimal deformation from a single folding event. This asymmetry suggests the presence of residual stress and strain, as fibers predominantly shifted in one direction, as shown in Fig. 10(c). During tensile loading, fibers could not straighten uniformly, which led to reduced collective load-bearing capability. A minor increase in tortuosity τ was observed, with the average rising from 1.0105 to 1.0146, and the maximum from 1.0188 to 1.0566. Inside filaments exhibited greater tortuosity than perpendicular outside filaments, resulting in a more dispersed fiber distribution (Fig. 10(b)). Interestingly, in the unfolded region, the average τ was 1.0087, and the maximum was 1.0201 (see red and black curves in Fig. 10(b)). While the unfolded region's average tortuosity was lower than that of the outside folded region, its maximum tortuosity exceeded that of the folded outside region. This is likely due to initial defects in the selected area, such as uneven coating and pre-existing deformations in certain filaments, as evidenced by the less smooth surface in Fig. 9(g) and the presence of red segments in Fig. 10(e). After folding, the highly deformed outer segments were stretched. However, since the entire filament underwent deformation, the average tortuosity increased while the maximum value decreased compared to the unfolded state. For a straight line, $\tau = 1$. However, due to the thickness of the plane weave filaments, perpendicular filaments experience initial deformation, resulting in a $1 - \frac{1}{1.0087} = 0.86$ % reduction in chord length

even in the unfolded state. After folding, the average segment shortening increased to 1 - $\frac{1}{1.0146}$ = 1.44 %, representing a 67 % increase. This demonstrates that even small changes in τ correspond to significant proportional increases in fiber shortening. At the macroscale, a small increase in τ after monotonic folding led to a 16.6 % reduction in elastic modulus at the macroscale. No significant fiber fractures were observed in the deformed regions. However, the presence of internal residual stress and strain led to a 6.6 % decrease in ultimate tensile strength, albeit with a relatively smaller impact compared to the elastic modulus reduction.

4.3. Folding endurance test

For many applications, membranes undergo multiple folding and unfolding cycles. To further investigate the effect of folding cycles on mechanical properties, folding endurance tests were conducted following the ISO 05626 standard. A MIT folding endurance tester (*Changjiang papermaking instrument co.LTD, Sichuan, China*) was used to fold the specimens to the designated number of cycles. The testing setup is shown in Fig. 11(b) and (c). Each specimen measured 85 mm × 15 mm and was folded at its midpoint to an angle of 135° under a 19.8 N force, at a speed of 175 ± 10 double folds per minute. Initially, a single specimen was tested to qualitatively observe crack development in the folded region, as illustrated in Fig. 11(a). Subsequently, multiple specimens were subjected to pre-determined folding cycles before undergoing tensile testing using the same *Wance* universal testing machine described in Section 4.1 (Fig. 7(a)). The objective was to evaluate the decline in tensile strength as a function of folding cycles. Tensile tests were conducted at a speed of 50 mm/min with a grip-to-grip separation of 30 mm.

As shown in Fig. 11(a), after 1,000 folding cycles, a noticeable white crease developed on the specimen; however, no significant structural damage was observed. After 5,000 cycles, the crease had widened further. From 10,000 cycles onward, visible cracks began to form along the crease, progressively expanding as the number of cycles increased. Additionally, the transverse fibers started to slide laterally, while the longitudinal fibers exhibited significant deformation. At 60,000 cycles, the transverse fibers at the crease had completely migrated out of the folding region, leaving only the longitudinal fibers in place. Although the longitudinal fibers were significantly bent, no obvious fractures were observed, suggesting that the material retained some load-bearing capacity in the longitudinal direction. To further explore the changes in mechanical properties, tensile tests were conducted on the folded specimens. Since the folding endurance tests did not provide direct force measurements, tensile testing was employed post-folding to evaluate mechanical degradation. The specimens used for tensile testing were the same ones subjected to the folding endurance test, rather than standard tensile test specimens. While this approach introduces some size-related effects, it remains highly effective for analyzing overall trends in mechanical performance.

Fig. 12 illustrates the force–displacement and stress–strain curves of fabric specimens subjected to different folding cycle counts. Table 3 summarizes the tensile test results, including elastic modulus, ultimate stress, and ultimate load (average value of three specimens of each group) after the folding endurance tests. The folding cycle count is

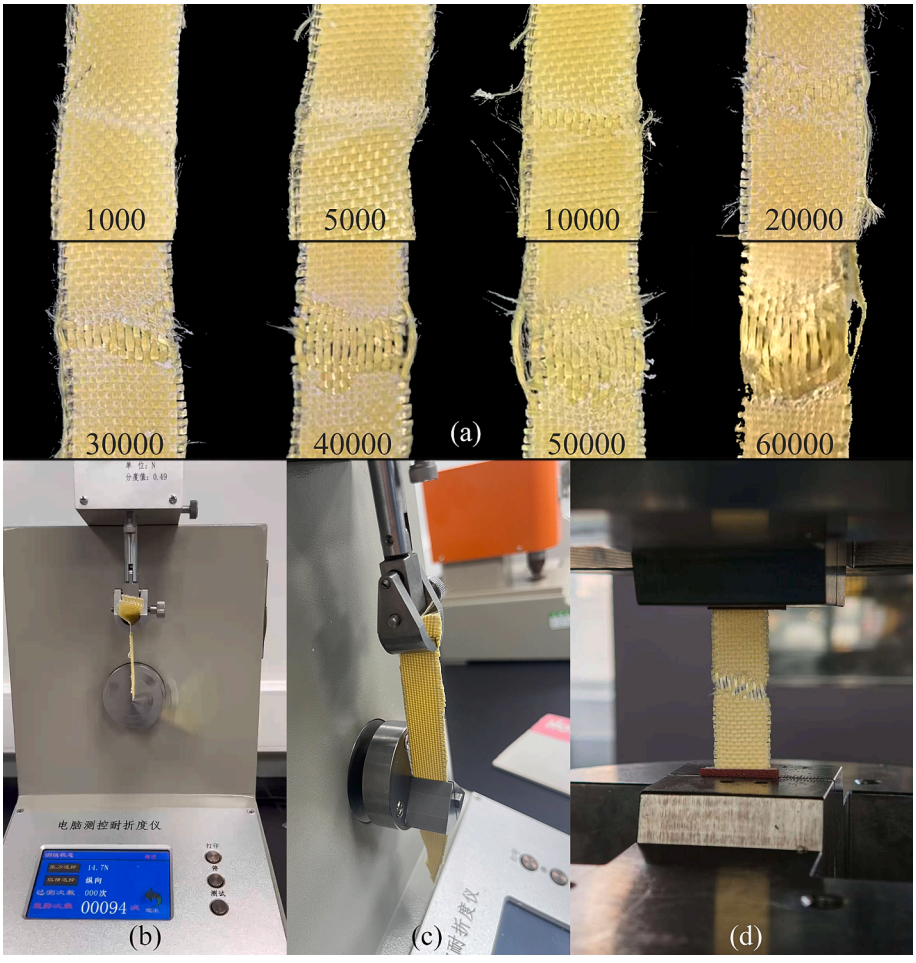

Fig. 11. Test setups:(a) folding part observation of one specimen after 1000, 5000, 10000, 20000, 30000, 40000, 50000, and 60,000 folding cycles; (b) and (c) folding endurance test and setup; (d) tensile test on a folded specimen.

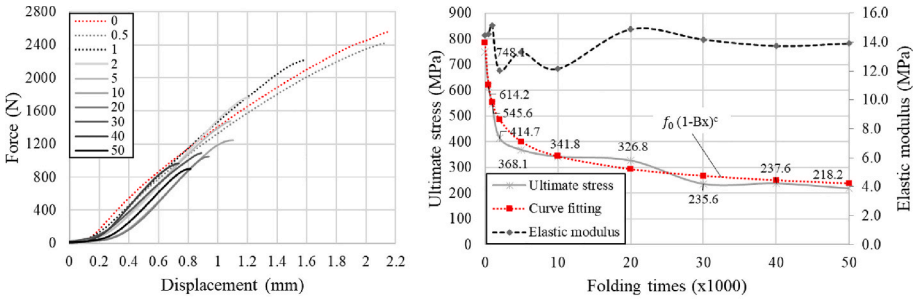

Fig. 12. Tensile test of folded specimens after folding endurance tests: (a) Force vs. Displacement; (b) Folding times vs. mechanical properties (elastic modulus and ultimate stress).

Table 3
Tensile test results of folded specimens after folding endurance tests: elastic modulus, ultimate stress, and ultimate load (average value of three specimens of each group).

Folding times (x1000)	Modulus E (GPa)	Ultimate Stress σ_{UIT} (MPa)	Ultimate Load F_{UIT} (kN)
0 (unfolded)	14.5	748.1	2.60
0.5	14.6	614.2	2.23
1	15.2	545.6	2.13
2	12.0	414.7	1.77
5	13.3	368.1	1.38
10	12.2	341.8	1.32
20	14.9	326.8	1.08
30	14.2	235.6	0.92
40	13.7	237.6	0.96
50	13.9	218.2	0.77

expressed in thousands (e.g., "50″ represents 50,000 folds). Groups with 1, 2, 5, 10, 20, 30, 40, and 50 cycles were tested, each with three specimens, while an unfolded group (0 cycles) served as the reference. Fig. 12(a) primarily illustrates the trend of each group of curves. For clarity, a representative specimen was selected from each group for plotting. After folding, the ultimate force decreased, while the elastic modulus (slope) remained relatively stable. For folded specimens, the post-peak decline was gradual upon rupture of all longitudinal fibers, whereas the unfolded specimens showed a sudden drop. To further quantify changes in ultimate stress and elastic modulus (calculated over the 1.5 %-1.8 % strain range), Table 3 presents the average values for three specimens per group. After 500 folds, the ultimate stress decreased by 19 % (from 748.1 MPa to 614.2 MPa). The most significant stress reduction occurred within the first 2000 cycles, followed by a slower decline between 2000 and 5000 cycles. After 10,000 folds, strength continued to decrease but at a reduced rate. By 50,000 folds, the material retained 29 % of its original strength, with visible creasing and relaxation but no significant rupture of longitudinal fibers, confirming the excellent toughness of Kevlar fibers. In practical applications, folding angles will not be as repetitive as in the experiments, and the folding cycles will be fewer than 500. Design considerations should incorporate sufficient safety margins based on these results.

According to classical fatigue theory, materials subjected to repeated loading below their ultimate strength will eventually experience fatigue failure. This behavior can be described by the empirical equation:

$$\sigma^m N = C.f_0 = C^{-m} \tag{13}$$

where σ is the applied fatigue stress, N is the fatigue life (number of cycles to failure), C and m are material-dependent fatigue constants, f_0 represents the initial ultimate strength.

For the constant-strain fatigue condition studied in this work, assuming that the elastic modulus E remains unchanged before and after fatigue, the corresponding fatigue relationship can be expressed as:

$$\varepsilon^m N = A \tag{14}$$

where ε is the applied fatigue strain, N is the fatigue life, m is the fatigue exponent, $A=C/E^m$ is a material-dependent fatigue constant. According to Miner's rule, which considers the cumulative effect of fatigue damage, the total damage fraction must satisfy:

$$\sum \frac{n_i}{N} \leq 1 \tag{15}$$

For a two-level loading (N_1 and N_2) scenario, after n_i cycles:

$$\frac{n_i}{N_1} + \frac{1}{N_2} = 1 \tag{16}$$

where considering the remaining load-carrying capacity f_r, the relationship can be derived as:

$$\frac{\varepsilon^m}{A} n_i + \frac{f_r^m}{C} = 1 \tag{17}$$

The downward trend of the curve can be fitted with the following equation:

$$f_r = (C - \sigma^m n_i)^{-m} = f_0(1 - Bn_i)^{-m} \tag{18}$$

where the coefficients with 95 % confidence bounds are B = -3.477 and$m$ = 0.2308 for this testing. B is a parameter related to material property. f_0 is the unfolded ultimate stress σ_{UIT} = 748.1 MPa.

The trends of these parameters with folding cycles are plotted in Fig. 12(b), where the x axis represents the n_i folding cycles. The computed modulus fluctuated around 14 GPa, which indicated that repeated folding had little effect on the material's modulus. The study provides valuable insights into the observed phenomena and quantitative analysis. Modulus and stress fluctuations for folded groups were greater than those from the uniaxial tensile tests. This variability arises from differences in the folding conditions for each specimen—sometimes folds occurred between two parallel fibers, other times on fibers, or at an angle to transverse fibers, affecting multiple layers of filaments.

For the elastic modulus, no softening phenomenon was observed, unlike in the tensile tests. This may be because a single fold typically induces localized plastic deformation or interface damage. After multiple folding cycles, the damage might gradually spread and become evenly distributed around the adjacent areas, rather than concentrating in a single folded region. This distribution averages out the localized softening effect, masking the significant stiffness reduction seen after a single fold. Residual stress from a single fold reduces stiffness in the deformed region, but after many folding cycles, the residual stress may dissipate or redistribute, stabilizing the overall stiffness and reducing the softening effect from individual folds. In addition, residual stress from a single fold reduces stiffness in the deformed region, but after

many folding cycles, the residual stress may dissipate or redistribute, stabilizing the overall stiffness and reducing the softening effect from individual folds. The stiffness of coated fabrics is primarily determined by fiber orientation. During repeated folding, fibers may undergo slight rearrangements, maintaining a relatively stable number of load-bearing fibers in the stretching direction and offsetting some of the softening effects. Finally, the calculated values for the elastic modulus are influenced by the selected strain range, which varies for each specimen's linear segment, introducing some human factors and randomness. However, the overall conclusion is that repeated folding has a minimal effect on the stiffness of this material.

4.4. Temperature variation: Dynamic mechanical analysis (DMA) tests

4.4.1. Experimental setup

The dynamic mechanical analysis (DMA) tests were carried out using a Q850 instrument (*TA Instruments*, *USA*), as depicted in Fig. 13(a). The configuration employed for the tensile mode of the DMA tests can be seen in Fig. 13(b), where a rectangular specimen is clamped. DMA serves as a technique to quantify the complex modulus encompassing both the storage modulus (É) and the loss modulus (E), which respectively represent the energy stored in the elastic part and the energy dissipated as heat due to friction. Tan δ, also known as the damping factor or loss tangent, is computed from the ratio of loss modulus (E) to the storage modulus (É).

In the conducted tests, a multi-frequency-strain test was conducted with an oscillatory strain amplitude of 10 μm. The frequencies spaced logarithmically, ranging from 0.32 Hz to 30 Hz, with two points per decade (0.32 Hz, 1 Hz, 3 Hz, 10 Hz, and 30 Hz). Throughout each test, the temperature was increased at a constant rate of 1 °C/min from −140 °C to 150 °C. In this test, the glass transition temperature (T_g) of the materials was determined from peak Tan δ values at 1 Hz.

4.4.2. Test results

Fig. 14 presents the DMA results for SC-AF. With an increase in loading frequency, the E', E, and Tan δ curves exhibited rightward shifts with slightly increased amplitudes. Previous research has highlighted the significance of material damping in vibration suppression, where T_g represents the peak of the Tan δ curve at 1 Hz. In the case of the SC-AF used for folding, the focus shifts to stiffness variation. Therefore, T_g is determined as the peak of the loss modulus curve, which occurs at approximately −50 °C. Fig. 14(a) demonstrates a substantial increase in stiffness of the material below T_g = -50 °C. To gain further insights into the viscoelastic properties of the material, a viscoelastic model was established. Characterizing this model necessitates two curves: the shift factor curve and the master curve [23]. The shift factor curve accounts for the change in stress relaxation rate with temperature, while the master curve illustrates variations in storage modulus across a wide range of frequencies and temperatures. Fig. 14(b) illustrates the constructed master and shift factor curves. The dashed lines encompass the storage moduli measured within the frequency range of 0.30 Hz to 10 Hz and the temperature range of −80 °C to 60 °C. Data at 30 Hz exhibited significant noise and was excluded from constructing the viscoelastic material model. At the reference temperature −20 °C, the shift factor is set to 1. By employing the shift factor curve, moduli at different temperatures and/or frequencies, which were not directly measured through DMA, can be obtained by shifting along the frequency axis.

During the construction of lunar bases at the lunar south pole, where temperatures can reach as low as 110 K (−163 °C) [33], when the inflatable structure is inflated and erected, temperature control becomes crucial when inflating and erecting inflatable structures. This is because extremely low environmental temperatures below T_g can impede the folding process. In such cases, it is highly desirable to employ coating materials or resins with lower T_g, such as high-phenyl silicone and fluorine rubbers. These materials offer improved flexibility and ease of folding in extremely cold conditions. However, it is important to highlight that the primary focus of this study is on the conceptual design of rigidizable inflatable habitats. While the research findings are applicable to lunar surface scenarios, their relevance extends beyond the lunar environment to other extreme locations like polar regions and high plateaus. The coating material described in this study, when combined with aramid fiber fabric, demonstrates an exceptional resistance to temperatures ranging from −35 to 250 °C. Such a combination renders it highly suitable for application in these extreme terrestrial environments.

5. Structural validation: SMP-based rigidizable inflatable habitats

5.1. Numerical model of variable stiffness skin: Temperature-based three stage stiffness

The finite element modeling (FEM) study presented in this section was carried out using Ansys Workbench. Before conducting structural simulations, it was necessary to establish the FEM material models for the restraint and rigidization materials. In previous studies, SMP was defined as a thermo-elastic material, focusing primarily on stiffness variation, while flexible AFRP was treated as a linear elastic material [32]. However, the effect of temperature on the stiffness of the restraint material was not considered, despite DMA tests indicating significant temperature dependence, especially in extremely low-temperature

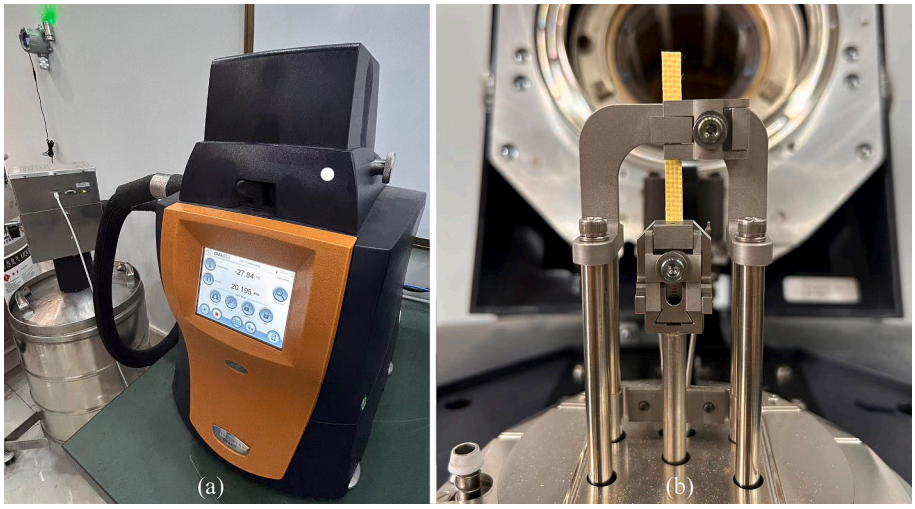

Fig. 13. DMA test setups: (a) Q850 (TA instruments, USA); (b) specimen in clamp using a DMA tensile mode.

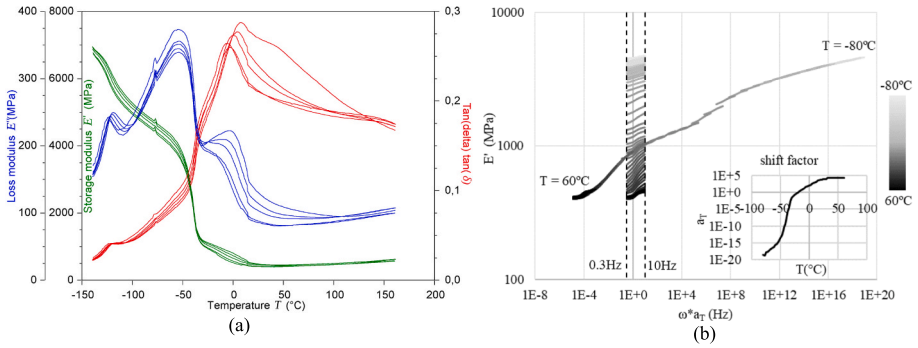

Fig. 14. DMA results: (a) storage modulus, loss modulus, and Tan δ vs. temperature; (b) master curve and shift factor.

conditions. Additionally, previous research did not fully account for the orthotropic nature of the materials. The rigidization SMP layer serves both as a rigidization element and a shape-control mechanism, particularly in space structures requiring precise shape control [22]. Given the large temperature variations on the Moon's surface (ranging from −180 °C to 130 °C at the equatorial region [26]), this study considers the state transitions of both the restraint material SC-AF ($T_g^{SC-AF} = -50$ °C) and the rigidization SMP material ($T_g^{SMP} = 65$ °C). The composite membrane material consists of 5 mm SC-AF and 5 mm SMP, with three stiffness states for structural simulation defined as follows:

- **State 1 (Extremely low temperature, −180 °C ~ − 50 °C):** Both SC-AF and SMP remain in the glassy state, making the skin material highly rigid. This condition is optimal for in-service applications on the lunar surface.
- **State 2 (Room temperature, 0 ~ 40 °C):** SC-AF transitions to a rubbery state while SMP remains in the glassy state, representing the most common condition. This configuration is typically used for the rigidization of flexible structures on Earth, requiring no additional temperature control.
- **State 3 (High temperature, >85 °C):** Both SC-AF and SMP enter the rubbery state, resulting in a highly flexible membrane material that can be deployed. This state often requires temperature control and activation energy, facilitating structural shape reconfiguration, such as inflation-based deployment or large deformation adjustments.

Based on these three states, corresponding stiffness matrices were defined for structural simulations. At room temperature, the single-layer SC-AF material was characterized as an orthotropic material, with the Young's modulus in the X-direction determined as 12.2 GPa based on previous tensile tests. In contrast, the Z-direction, primarily influenced by the resin—specifically the silicone coating—was estimated at 2 MPa. The Poisson's ratio in the XY plane was predominantly governed by the fiber fabric, while the Poisson's ratios in the YZ and XZ planes were dictated by the resin material, with values of 0.05, 0.47, and 0.47, respectively. The shear moduli in these three directions were 1000 MPa, 0.68 MPa, and 0.68 MPa, respectively. At low temperatures, the modulus of the silicone coating was defined as 2 GPa, reflecting a stiffness change of approximately 1000 times when transitioning from the glassy to the rubbery state. The X-direction modulus increased to 13.2 GPa. Poisson's ratios in the YZ and XZ planes were adjusted to 0.05, 0.35, and 0.35, while the shear moduli were modified to 1000 MPa, 740 MPa, and 740 MPa, respectively. For tensile loading in inflatable structures, a four-layer stacking sequence was adopted to enhance isotropic properties. The material properties were derived using CLT within the ACP module of Ansys Workbench. The laminate stiffness values were computed based on a [0F/45F2/0F] stacking sequence and used to define the orthotropic material. The laminate stiffness values included $E_1 = E_2 = 8.90$ GPa and $G_{12} = 3.40$ GPa when the silicone coating was flexible, while in the glassy state, the values increased to $E_1 = E_2 = 9.56$ GPa and $G_{12} = 3.64$ GPa. Considering the reduced stress resistance in non-fiber directions, the final ultimate stress was set at 50 % of the single 0° layer, resulting in a limit stress of 312 MPa for the simulation.

Using these defined material states, the ACP module was employed to design the layered structure, consisting of a 5 mm multi-layer SC-AF composite combined with a 5 mm thermo-elastic SMP layer. The resulting three material models were used for structural simulations.

5.2. Stiffness variation based on the dual-layer beam model

To validate the rigidization capacity of the three membrane material models, a simply supported dual-layer beam (500 mm*50 mm) was modelled in Ansys Workbench. The upper layer comprised five laminates with a [0F/45F2/0F] stacking sequence with a total thickness of 5 mm, while the lower layer consisted of a 5 mm thick thermo-elastic SMP. The multi-layer SC-AF model was simplified as an orthotropic material with several simplifying assumptions. The influence of ply stacking sequence and thickness distribution on global stiffness was homogenized, effectively averaging individual ply contributions. The coupling between in-plane forces and bending moments (B-matrix in classical lamination theory) was omitted, as the symmetric and balanced laminate ensured B = 0. The flexural stiffness matrix (D-matrix) was incorporated into the orthotropic approximation without explicitly considering interlayer bending effects. This approach eliminated extension-bending coupling and simplified computations, through it inherently neglected localized anisotropy from ply orientations (e.g., 45° layers), interlaminar shear effects, and through-thickness property gradients.

The beam was subjected to a 5 N mid-span load. Table 4 presents the mid-span deflections for the three material states, quantifying stiffness variation using the most flexible state as a reference. In the flexible state, the mid-span deflection was 7.48 mm. After rigidization, the equivalent beam stiffness increased by a factor of 4.23, and in the extreme low-temperature condition—where the restraint layer's coating transitioned to the glassy state—the stiffness increased by 7.68 times. Additionally, an intermediate case (*) was analysed, where the upper SC-AF layer's coating was in the glassy state while the lower SMP remained rubbery. Though this specific condition was not achievable with the selected materials, it could be realized with materials possessing different T_g ranges. The results indicate that the rigidization effect of the SMP layer was more pronounced than that of the coating, likely due to

Table 4
Mid-span deflection and stiffness variation for the three material states.

Material state	State 1 E_1^g &E_2^g	State 2 E_1^r &E_2^g	State 3 E_1^r &E_2^r	*E_1^g & E_2^r
Mid-span deflection (mm)	0.97	1.77	7.48	2.61
Stiffness variation	7.68	4.23	1	2.87

differences in volume and material properties. This suggests that the restraint layer could potentially be combined with a variable-stiffness resin, merging the restraint and rigidization layers into a single layer. However, in some configurations, the restraint layer may consist solely of fibre fabric without resin or coating [34], making a separate rigidization layer necessary. For applications where precise shape control is not required, other resins with significant stiffness variation could replace SMP, which serves as a specific case in this study.

5.3. Static analysis (considering stiffness variation of silicone coating)

This three-state material model was further validated through static analysis by comparing the structural behavior before and after rigidization under 1 atm internal pressure and air leakage. The semi-spherical structure had a diameter of 3 m and was buried 0.5 m underground with lunar regolith. The membrane comprised a 5 mm SMP layer and a 5 mm SC-AF restraint layer. The 3 m thick regolith layer exerted a uniform downward external pressure of 8.1 kPa on the Moon. The inflatable module maintained an internal pressure of 101 kPa under normal operating conditions. Other boundary conditions and material models followed previous studies [32], as illustrated in Fig. 15(a). For crewed lunar applications, maintaining an internal pressure of 1 atm is essential. The external regolith pressure actually helps counteract some inner pressure, reducing stress levels in the structure compared to scenarios without external pressure. However, in the event of air leakage, the overlying regolith load could pose a collapse risk. To assess structural safety and performance under these conditions, maximum deformation (D_{max} , typically at the top) and von Mises stress in (σ_{SC-AF} and σ_{SMP}) were selected as evaluation criteria. The von Mises stress serves as a suitable metric for comparing stress levels across different states rather than for failure prediction, given the high safety redundancy in the restraint layer design. Additionally, due to the near in-plane isotropy achieved through layup design, von Mises stress provides a representative measure of overall stress variation under different control states.

In the nonrigid state, the SMP-based structure exhibited a maximum deformation of 72.3 mm, with peak stresses of 113.3 MPa in the SC-AF material and 0.53 MPa in the SMP. After rigidization, the maximum deformation was reduced by 48 % to 37.6 mm, while the SC-AF peak stress decreased by 38 % to 72.1 MPa. The rigid SMP layer redistributed part of the load, increasing its own stress to 19.7 MPa. Considering the stiffening effect of the SC-AF silicone coating at extremely low temperatures (reference set at −100 °C), the maximum deformation further decreased to 37.1 mm, with a slight increase in SC-AF stress to 75.0 MPa, as the hardened coating enhanced material stiffness and assumed additional load. Fig. 15(b)~(d) compares the deformation contours across the three cases, highlighting that the rigidization layer provided the primary structural enhancement, while the coating stiffening effect served as a secondary reinforcement. During punctures, internal pressure P_1 dropped to zero while external pressure P_2 remained constant, leading to sudden buckling and numerical convergence failure due to excessive deformation. However, in the rigidized state under air leakage conditions ($P_1 = 0$), maximum deformation was significantly reduced to 13.7 mm, while peak equivalent stress in the SMP was limited to 6.12 MPa. At extremely low temperatures, further considering the stiffening effect of the silicone coating, the maximum deformation further decreased to 13.3 mm. If only the restraint material's coating hardened without a rigidization layer, the structure still failed to converge under the same simulation conditions, demonstrating that the coating effect alone could only provide auxiliary reinforcement and could not replace the rigidization layer. Detailed values of maximum deformation and stress in SC-AF and SMP for both nonrigid and rigidized cases under 1 atm internal pressure and air leakage conditions are reported in Table 5.

6. Discussion

This study investigates the feasibility of a rigidizable inflatable habitat, highlighting its advantages, material selection, and structural performance. Key considerations and future directions at the material and structural levels, including theoretical, experimental, and simulation studies, are outlined below:

Table 5
Rigid vs. nonrigid at $P_1 = 101$ kPa inner pressure and air leakage conditions: deformations and stresses.

Conditions		D_{max} (mm)	σ_{SC-AF} (MPa)	σ_{SMP} (MPa)
Normal operation $P_1 = 101$ kPa and $P_2 = 8.1$ kPa	Nonrigid (100 °C)	72.3	113.3	0.53
	Rigid (22 °C)	37.6	72.1	19.7
	Coating stiffening (−100 °C)	36.7	75.0	19.2
Reduction	Rigid vs. nonrigid	48 %	38 %	–
Air leakage $P_1 = 101$ kPa to 0 and $P_2 = 8.1$ kPa	Nonrigid (85 °C)	Unconverged	Unconverged	Unconverged
	Rigid (22 °C)	13.7	23.9	6.12
	Coating stiffening (−100 °C)	13.3	24.9	6.13

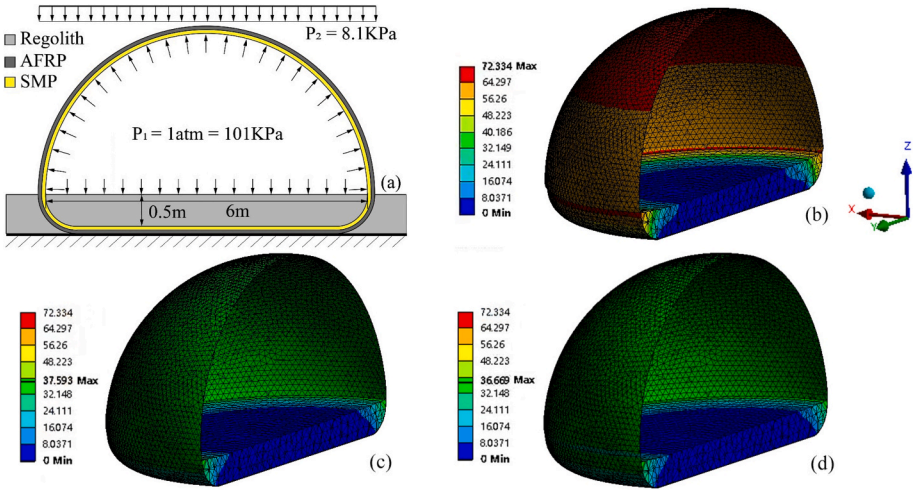

Fig. 15. Semi-sphere inflatable habitat with 1 atm inner pressure: (a) structure design and boundary conditions [32]; (b)~(d) deformation contours of rigid, nonrigid, and rigid with stiffened coating.

- **Theoretical model:** A theoretical model has been established to describe the stiffness variation of the dual-layer material, correlating the stiffness and thickness ratios of the two layers. It quantifies rigidization capability and load-bearing enhancement in the stiff state, and deformation capacity in the flexible state. However, assumptions in the model require further verification through numerical or experimental results. Despite its simplicity, the model provides a valuable design reference and foundation for further development. Future research will extend the model to various structural forms, boundary conditions, and geometric configurations to refine and optimize designs.
- **Application limits:** For rigidizing or reinforcing flexible layered materials, Material 2 primarily functions as a rigidizing role in this system. Material 1, a soft material, has a stiffness comparable to Material 2 in its flexible state ($E_1 \approx E_{2,min}$), while in its stiff state, Material 2 exhibited significantly higher stiffness ($E_{2,max} \gg E_1$). For vibration control, especially in structural frequency tuning, Material 2 primarily functions as a frequency-tuning element, while Material 1 bears the load. In this case, Material 1 should have a stiffness significantly greater than $E_{2,min}$ ($E_1 \gg E_{2,min}$) in the flexible state and at least on the same order of magnitude as $E_{2,max}$ ($E_1 \approx E_{2,max}$) in the rigid state, or even greater. If $E_1 \gg E_{2,max}$, the overall stiffness variation remains minor, limiting the frequency tuning effect. Previous research has demonstrated that by utilizing the variable stiffness and damping properties of SMP components (such as joints or sandwich plates), structural dynamic performance can be adjusted, enabling semi-active vibration control. Studies on truss bridges, frames, and sandwich plates have evaluated the efficiency of SMP-based control [23,35,36,37].However, a higher volume of SMP does not necessarily guarantee improved performance. Since this study primarily investigates variable stiffness components for large deformation shape control and rigidization, future research will further explore the impact of different design parameters—such as material distribution, component configuration, and material volume—on structural vibration control effectiveness.
- **Shape control and rigidization:** The concept enables stiffness variation to address different operational requirements across deployable, inflatable, and shape-morphing structures. Practical applications require careful consideration of specific conditions. For example, regarding a rigidizable lunar habitat, the conceptual design needs further refinement, such as optimizing connections, openings and folding patterns (e.g., folding a spherical structure). Given the high cost of lunar transportation, a trade-off between mass increase and rigidization/load-bearing capabilities must be evaluated to ensure cost-effectiveness. For other deployable structures, transitioning to a flexible state during shape reconfiguration to reduce activation energy and improve shape control precision [23]. Once the desired shape is achieved, the material rigidizes to enhance load-bearing capacity and ensure stability for subsequent applications.
- **Folding behavior and constitutive modelling:** Micro-CT analysis revealed that a single folding event causes fiber distribution asymmetry, filaments expanding, fibers bending, reduced fiber density, localized voids, and coating damage, leading to decreased fiber engagement and a 17 % stiffness reduction during tension tests. Increased average and maximum tortuosity further confirmed fiber deformation. To further investigate these effects, a statistical approach could be employed by analyzing multiple CT samples to establish a quantitative relationship between microscopic tortuosity and macroscopic properties such as elastic modulus and strength [38]. This study also suggests material design improvements for lunar inflatable structures, emphasizing isotropic properties to better withstand sustained pressure differentials. In isotropic materials, folding-induced stiffness changes may be less pronounced, as uniformly distributed fibers in multiple directions ensure more even load distribution, reducing the likelihood of significant stiffness changes caused by fibers shifting away from their load-bearing orientation during folding.
- **Folding endurance:** Strength degradation progressed rapidly within the first 2000 cycles, while the modulus stabilized after 50,000 folds. Notably, unfolded specimens in folding endurance tests (Table 3) exhibited higher modulus and stress values than those in uniaxial tensile tests (Table 2), likely due to size effects from non-standard specimen dimensions. The MIT folding endurance tester, typically used for less ductile materials like paper to determine breaking cycle numbers, lacks load sensors and cannot track force per cycle. Beyond 10,000 cycles, results fluctuated significantly with significant variation among the three specimens, reducing measurement accuracy. Practical applications should guide testing parameters, such as folding cycle limits and angles. The $\pm$ 135° folding angle used here was constrained by testing equipment, whereas actual applications typically involve nearly 180° unidirectional folding. Additionally, this study measured post-fatigue strength, which shares similarities with fatigue testing. Future studies could incorporate specialized fixtures to achieve controlled folding angles and conduct dedicated folding fatigue tests to establish relationships between cycle count and mechanical performance. Despite the lack of dedicated instruments or standardized protocols, these experiments are valuable for observing trends, conducting preliminary quantification, and providing insights for further research.
- **Simulation Improvements:** This study refined structural simulations by employing an orthotropic anisotropic model to more accurately represent the behavior of membrane material. The SMP used in this study is a commercially available material designed for experimental conditions at room temperature on Earth. However, its applicability to the lunar environment remains uncertain due to the extreme temperature fluctuations. There is an urgent need for variable stiffness materials with a low glass T_g and a significant stiffness variation between the glassy and rubbery states to meet the demands of lunar applications. For the restraint material, if the resin remains in the glassy state under operational conditions, it could further enhance the structural load-bearing capacity. However, during deployment, the resin or coating must transition to the rubbery state to ensure flexibility and ease of unfolding. In specific scenarios, active temperature control may be required to facilitate these transitions. Alternatively, other activation methods for stiffness regulation could be explored as viable approaches. Note that the materials discussed in this study are not definitive solutions but rather illustrative examples for the proposed modeling approach. Future work should incorporate multibody dynamics, large deformation analysis, and process-based analyses for further validation.
- **Extreme environment adaptability and structural validation:** The impact of extreme conditions on the long-term performance of materials remains uncertain but is crucial for ensuring structural safety throughout their service life. For example, in the lunar environment, future research should examine material performance under extreme lunar conditions, including vacuum aging, temperature cycling, radiation exposure, dust abrasion, creep, and other degradation factors. Besides the material-level tests and structural-level simulation in this research, future work will involve structural-scale experiments with scaled-down prototypes (Fig. 16) to verify the folding and inflation process, rigidization capability, airtightness, and impact resistance. A construction demonstration is planned to verify the feasibility of the designed construction process.

7. Conclusion

The proposed rigidizable inflatable lunar habitat demonstrates strong potential by enabling stiffness variation to accommodate different requirements during transportation, construction, and service. For the SMP-based variable stiffness application in this study, the recommended thickness ratio t is 0.02 or 1, but should not exceed 5. The

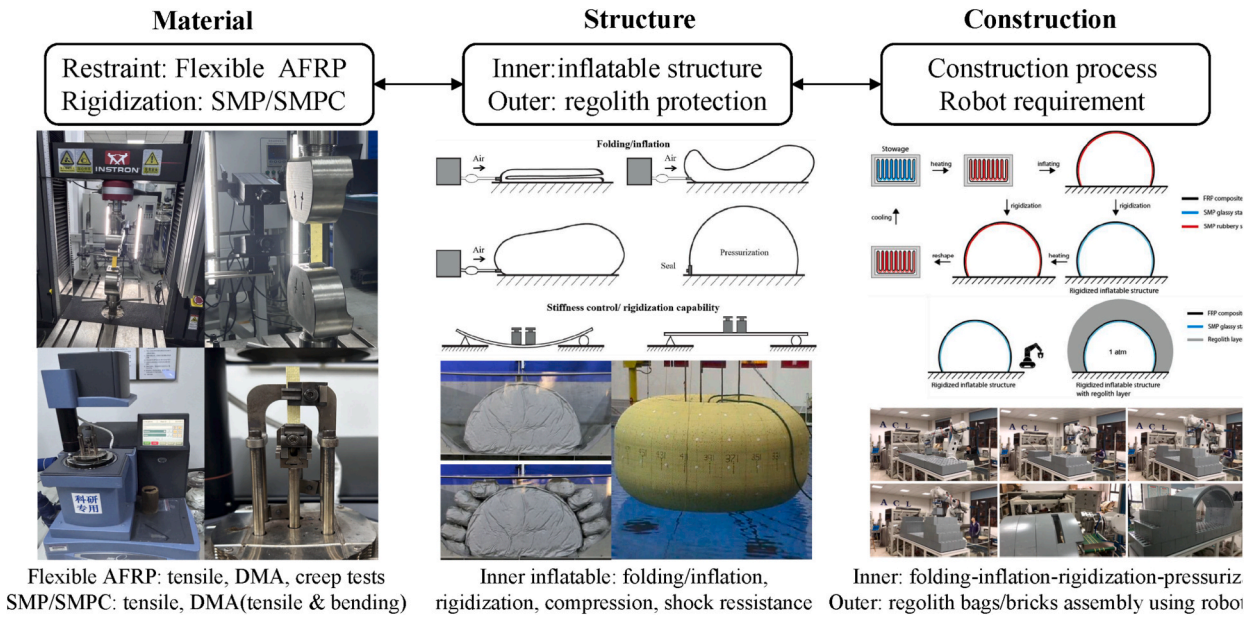

Fig. 16. Multi-level testing of rigidizable inflatable lunar habitat: material, structure, and construction [31].

designed rigidization capability should be tailored to the structural load-bearing requirements.

The newly developed SC-AF restraint material demonstrates high toughness and improved foldability with minimal strength degradation, making it suitable for repeated folding and sustained lunar surface pressure differentials. The observed reduction in tensile modulus after folding is attributed to microstructural damage, including fiber distribution asymmetry, decreased filament density, localized curvature/buckling, gap formation, and micro-cracks in silicone coating. These effects disrupt fiber alignment and engagement during loading, with softening dominated by deformation and misalignment rather than fiber breakage. After repeated folding, the modulus stabilizes, likely due to residual stress and strain redistribution. For reusable inflatable structures, a 20 % design safety margin is recommended within the first 500 cycles of normal operations.

Numerical simulations validate the feasibility of rigidizable inflatable habitats and advance a three-state membrane material model. Results suggest that with optimized material selection and layout, the rigidization and restraint functions may be integrated into a single layer, reducing mass and volume without sacrificing performance. This modeling approach enhances the prediction accuracy for structural behavior under varying lunar thermal conditions, providing a foundation for future inflatable designs in extreme environments.

Further studies should focus on developing materials with greater stiffness variation and faster activation capabilities. Additionally, extreme environmental adaptability of these materials should be explored, including vacuum aging, thermal cycling, radiation degradation, micrometeoroid impact resistance, and creep behavior. Large-scale physical model tests should be conducted to verify structural integrity, operational safety, and deployment feasibility in real-world applications [31].

CRediT authorship contribution statement

Qinyu Wang: Writing – review & editing, Writing – original draft, Visualization, Validation, Software, Resources, Project administration, Methodology, Investigation, Funding acquisition, Formal analysis, Conceptualization. **Peng Feng:** Validation, Supervision, Resources, Project administration, Methodology, Conceptualization. **Bo Wu:** Visualization, Validation, Investigation, Formal analysis. **Jiacheng Zhao:** Validation, Investigation, Formal analysis. **Juntian Tang:** Validation, Formal analysis. **Kaspar Jansen:** Validation, Methodology, Conceptualization.

Declaration of competing interest

The authors declare that they have no known competing financial interests or personal relationships that could have appeared to influence the work reported in this paper.

Acknowledgments

This research project has been supported by National Natural Science Foundation of China (52308265), 17th China Postdoctoral Science Foundation Fellowship (2024T170487), China Postdoctoral International Exchange Program (YJ20220280), Shuimu Tsinghua Scholar Program, Key Technologies R&D Program of CNBM (JT_CORE-202311-000012), and Xplorer Prize.

Appendix A

A.2 Numerical verification of dual-layer beam

To validate the theoretical stiffness model in Section 3, a simply supported dual-layer beam with a length of 500 mm and a width of 50 mm was modelled in Ansys Workbench. The beam consists of Material 1 with an elastic modulus $E_1 = 3.3$ MPa and a thickness of 5 mm, subjected to a 0.01 N mid-span load. The stiffness variation under small deformation was evaluated by comparing the mid-span deflection ratios under the same load. The finite element analysis (FEM) results demonstrate excellent agreement with the theoretical predictions for small deformations, as summarized in Table A. 1, with the maximum error being only 0.414 % even as the thickness ratio increases.

Table A1
Comparison of SMP dual-layer beam's stiffness variation: theory vs. simulation.

Thickness ratio $t = h_2/h_1$	2 %	1	2	3	4	5
Mid-span deflection (stiff) (mm)	4.0069	1.8950	0.5627	0.2381	0.1224	0.0712
Mid-span deflection (flexible) (mm)	14.259	0.0361	0.0046	0.0014	0.0006	0.0003
Stiffness variation (simulation)	3.559	52.45	121.59	172.53	209.24	236.58
Stiffness variation (theory)	3.56	52.4	121.5	172.2	208.6	235.6
Error (%)	−0.039	0.100	0.078	0.193	0.307	0.414

For large deformations in the flexible state, the FEM results were compared with the theoretical predictions in Fig. 5, with detailed results presented in *Figure A. 1.*The red curves represent the theoretical results, while the black curves represent the simulation results. The comparison shows excellent agreement in both the angle and x-direction displacement. For the y-direction displacement, the agreement is strong initially but deviates as the load increases, reaching approximately 20 % error at 5 N. This discrepancy is primarily caused by differences in numerical solution methods (as the governing equations cannot be solved directly) and may also be influenced by nonlinear geometric effects, boundary conditions, and material assumptions. Despite this, the overall results confirm the model's accuracy across both small and large deformation regimes.

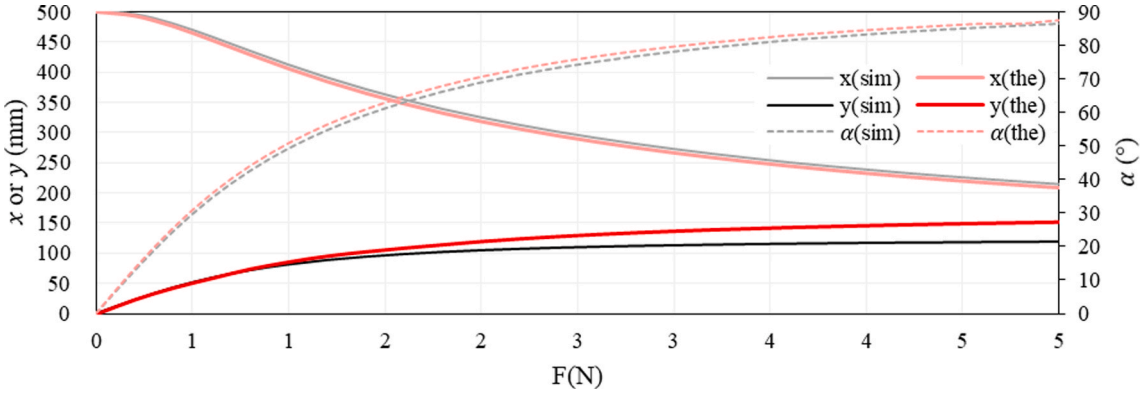

Fig. A1. Theory vs. Simulation: SMP dual-layer beam under large deformation.

Data availability

Data will be made available on request.

References

[1] Ruess F, Schaenzlin J, Benaroya H. Structural design of a lunar habitat. J Aerosp Eng 2006;19(3):133–57. https://doi.org/10.1061/(ASCE)0893-1321(2006)19:3(133).

[2] Smith M, Craig D, Herrmann N, Mahoney E, Krezel J, McIntyre N, et al. The artemis program: an overview of nasa's activities to return humans to the moon. 2020 IEEE Aerospace Conference 2020:1–10. https://doi.org/10.1109/AERO47225.2020.9172323.

[3] Song J. China emphasizes international cooperation in future lunar and deep space exploration. Retrieved from Bull Chin Acad Sci 2019;2:72–9. http://www.bcas.cas.cn/issue/2019_02/.

[4] Flahaut J, van der Bogert C, Crawford I, Vincent-Bonnieu S. Scientific perspectives on lunar exploration in Europe. npj Microgravity 2023;9:50. https://doi.org/10.1038/s41526-023-00298-9.

[5] H. Sasaki, J. Director, JAXA's Lunar exploration activities, Proceedings of the 62nd Session of COPUOS. (2019) 12 - 21. Retrieved from https://www.unoosa.org/.

[6] Hoshino T, Wakabayashi S, Ohtake M, Karouji Y, Hayashi T, Morimoto H, et al. Lunar polar exploration mission for water prospection-JAXA's current status of joint study with ISRO. Acta Astronaut 2020;176:52–8. https://doi.org/10.1016/j.actaastro.2020.05.054.

[7] An HJ. South Korea's Space Program. Asia Policy 2020;15(2):34–42. https://doi.org/10.1353/asp.2020.0029.

[8] Rousek T, Eriksson K, Doule O. SinterHab. Acta Astronaut 2012;74:98–111. https://doi.org/10.1016/j.actaastro.2011.10.009.

[9] Cesaretti G, Dini E, De Kestelier X, Colla V, Pambaguian L. Building components for an outpost on the Lunar soil by means of a novel 3D printing technology. Acta Astronaut 2014;93:430–50. https://doi.org/10.1016/j.actaastro.2013.07.034.

[10] Zhou C, Chen R, Xu J, Ding L, Luo H, Fan J, et al. In-situ construction method for lunar habitation: Chinese Super Mason. Autom Constr 2019;104:66–79. https://doi.org/10.1016/j.autcon.2019.03.024.

[11] Bao C, Zhang D, Wang Q, Cui Y, Feng P. Lunar in situ large-scale construction: quantitative evaluation of regolith solidification techniques. Engineering 2024;39:204–21. https://doi.org/10.1016/j.eng.2024.03.004.

[12] Qi H, Yang M, Zhang X, Zhang Y, Wu B, Liu J. Review on the structural design and materials of covers for inflatable lunar habitat. Spacecraft Environ Eng 2021;38(6):715–22.

[13] Cassapakis C, Thomas M. Inflatable structures technology development overview. Space programs and technologies conference. 1995.

[14] Benaroya H. Lunar habitats: a brief overview of issues and concepts. Reach 2017;7:14–33. https://doi.org/10.1016/j.reach.2018.08.002.

[15] Ulubeyli S. Lunar shelter construction issues: the state-of-the-art towards 3D printing technologies. Acta Astronaut 2022;195:318–43. https://doi.org/10.1016/j.actaastro.2022.03.033.

[16] Bowling L, Horvath B, Wohl C. Integration of Advanced Structures and Materials Technologies for a Robust Lunar Habitat. 2021 IEEE Aerospace Conference 2021;50100. https://doi.org/10.1109/AERO50100.2021.9438355.

[17] Defoort B, Peypoudat V, Bernasconi MC, Chuda K, Coqueret X. Recent advances in the rigidization of gossamer structures. Textile Compos Inflatable Struct 2005:259–83. https://doi.org/10.1007/1-4020-3317-6.

[18] Schenk M, Viquerat AD, Seffen KA, Guest SD. Review of inflatable booms for deployable space structures: packing and rigidization. J Spacecr Rocket 2014;51(3):762–78. https://doi.org/10.2514/1.A32598.

[19] Liu Y, Du H, Liu L, Leng J. Shape memory polymers and their composites in aerospace applications: a review. Smart Mater Struct 2014;23(2):023001. https://doi.org/10.1088/0964-1726/23/2/023001.

[20] Sokolowski W, Tan S, Willis P, Pryor M. Shape memory self-deployable structures for solar sails. Smart Materials 2008;7267:104–17. https://doi.org/10.1117/12.814301.

[21] Sokolowski W, Tan S, Pryor, M. Lightweight shape memory self-deployable structures for gossamer applications. 45th AIAA/ASME/ASCE/AHS/ASC Structures, Structural Dynamics & Materials Conference. 1660; 2004. doi: 10.2514/6.2004-1660.

[22] Lin J, Knoll C, Willey C. Shape memory rigidizable inflatable (RI) structures for large space systems applications. 47th AIAA/ASME/ASCE/AHS/ASC Structures, Structural Dynamics, and Materials Conference 14th AIAA/ASME/AHS Adaptive Structures Conference 7th. 1896; 2006. doi: 10.2514/6.2006-1896.

[23] Wang Q, Senatore G, Jansen K, Habraken A, Teuffel P. Design and characterization of variable stiffness structural joints. Mater Des 2020;187:108353. https://doi.org/10.1016/j.matdes.2019.108353.

[24] Wang Q, Feng P, Jansen, K. Material design optimization of restraint layer for rigidizable inflatable lunar habitats, 12th International Conference on Fiber-Reinforced Polymer (FRP) Composites in Civil Engineering, Lisbon. (2025). "in press".

[25] Heinicke C, Arnhof M. A review of existing analog habitats and lessons for future lunar and Martian habitats. REACH 2021;21:100038. https://doi.org/10.1016/j.reach.2021.100038.
[26] Bao C, Feng PZD, Wang Q, Yang S. Conceptual design and experimental investigation of regolith bag structures for lunar in situ construction. J Build Eng 2024;95:110245. https://doi.org/10.1016/j.jobe.2024.110245.
[27] De la Fuente H, Raboin J, Valle G, Spexarth G. TransHab-NASA's large-scale inflatable spacecraft. 41st Structures, Structural Dynamics, and Materials Conference and Exhibit. 1822; 2000. doi: 10.2514/6.2000-1822.
[28] Shaobo Y, Peng F, Daobo Z, Yang Z, Junfeng Q, Charun B, et al. Research on simulated lunar soil solar concentrator melting experiment for in-situ construction on lunar surface (in Chinese). In: Huazhong Keji Daxue Xuebao (Ziran Kexue Ban)/Journal of Huazhong University of Science and Technology (Natural Science Edition); 2024. p. 130–8.
[29] Rocha J, Sena-Cruz J, Pereira E. Influence of adhesive stiffness on the post-cracking behaviour of CFRP-reinforced structural glass beams. Compos B Eng 2022;247:110293. https://doi.org/10.1016/j.compositesb.2022.110293.
[30] Feng P, Zhao J, Wang Q, Zhai J, Zhou P. Self-shaping free-form spatial structure with large-deformable bunched CFRP rods. Eng Struct 2024;316:118565. https://doi.org/10.1016/j.engstruct.2024.118565.
[31] Wang Q, Feng P, Jansen, K. Designs of self-rigidizable inflatable habitats for construction in extreme environments, Proceedings of the IASS 2024 Symposium, Zurich. (2024). Retrieved from https://app.iass2024.org/.
[32] Wang Q, Feng P, Jansen K, Charun B. A novel rigidizable inflatable lunar habitation system: design concept and material characterization. Mater Des 2024;246:113289. https://doi.org/10.1016/j.matdes.2024.113289.
[33] Williams J, Greenhagen B, Paige D, Schorghofer N, Sefton-Nash E, Hayne P, et al. Seasonal polar temperatures on the Moon. J Geophys Res Planets 2019;124(10):2505–21. https://doi.org/10.1029/2019JE006028.
[34] Valle GD, Litteken D, Jones, TC. Review of habitable softgoods inflatable design, analysis, testing, and potential space applications. AIAA Scitech 2019 Forum. 1018; 2019. doi: 10.2514/6.2019-1018.
[35] Wang Q, Senatore G, Jansen K, Habraken A, Teuffel P. Seismic control performance of a three-story frame prototype equipped with semi-active variable stiffness and damping structural joints. Earthquake Eng Struct Dynamics 2021;50(13):3379–402. https://doi.org/10.1002/eqe.3514.
[36] Wang Q, Senatore G, Jansen K, Habraken A, Teuffel P. Variable stiffness and damping components for semi-active vibration control and inflatable rigidization. Proceedings of the ABSE Symposium Manchester 2024;2024:534. https://doi.org/10.2749/manchester.2024.0534.
[37] Wang Q, Senatore G, Jansen K, Habraken A, Teuffel P. Vibration suppression through variable stiffness and damping structural joints. Front Built Environ 2020;6:550864. https://doi.org/10.3389/fbuil.2020.550864.
[38] Zhou P, Feng P, Qiu J. Analysis of the tensile behavior of FRP textile for multi-scale fiber reinforced cementitious composite. Cem Concr Compos 2024;147:105416. https://doi.org/10.1016/j.cemconcomp.2023.105416.